Mapping cellular targets of covalent cancer drugs in the entire mammalian body

Authors: Zhengyuan Pang[1, 2,10], Verina H. Leung[1,10], Cailynn C. Wang[1], Ahmadreza Attarpour[3,4], Anthony Rinaldi[3], Hanbing Shen[1], Maria Dolores Moya-Garzon[5, 6], Logan H. Sigua[1], Claire Rammel[7], Alexandra Selke[1], Christopher Glynn[1], Melaina Yender[1], Senhan Xu[1], Javid J. Moslehi[7], Peng Wu[8], Jonathan Z. Long[5], Maged Goubran[3,4,9], Benjamin F. Cravatt[2], Li Ye [1, 11*]

[1]Howard Hughes Medical Institute, Department of Neuroscience, Dorris Neuroscience Center, The Scripps Research Institute, La Jolla, California, 92037, United States.

[2]Department of Chemistry, The Scripps Research Institute, La Jolla, California, 92037, United States.

[3]Physical Sciences Platform, Sunnybrook Research Institute, Toronto, Ontario, Canada.

[4]Department of Medical Biophysics, University of Toronto, Toronto, Ontario, Canada.

[5]Department of Pathology, Stanford School of Medicine, Stanford, CA, USA

[6]Sarafan ChEM-H, Stanford University, Stanford, CA, USA

[7]Section of Cardio-Oncology & Immunology, Cardiovascular Research Institute (CVRI), University of California San Francisco, School of Medicine, San Francisco, California, 94158, United States.

[8]Department of Molecular and Cellular Biology, The Scripps Research Institute, La Jolla, California, 92037, United States.

[9]Hurvitz Brain Sciences, Sunnybrook Health Sciences Centre, Toronto, Ontario, Canada.

[10]These authors contributed equally.

[11]Lead contact

*Correspondence: liye@scripps.edu

SUMMARY:

As our understanding of biological systems reaches single-cell and high spatial resolutions, it becomes imperative that pharmacological approaches match this precision to understand drug actions. This need is particularly urgent for the targeted covalent inhibitors that are currently re-entering the stage for cancer treatments. By leveraging the unique kinetics of click reactions, we developed volumetric clearing-assisted tissue click chemistry (vCATCH) to enable deep and homogeneous click labeling across the 3D mammalian body. With simple and passive incubation steps, vCATCH offers cellular resolution drug imaging in the entire adult mouse. We combined vCATCH with HYBRiD imaging and virtual reality to visualize and quantify *in vivo* targets of two clinical cancer drugs, afatinib and ibrutinib, which recapitulated their known pharmacological distribution and revealed previously unreported tissue and cell type engagement potentially linked to off-target effects. vCATCH provides a body-wide, unbiased platform to map covalent drug engagements at unprecedented scale and precision.

KEYWORDS:

drug targets, tissue clearing, whole-body imaging, targeted covalent inhibitors

INTRODUCTION

The primary binding sites for drug molecules are critical determinants of drug efficacy and toxicity. Although molecular target identification strategies, such as chemoproteomics[1-5], chemogenomic[6-9], and thermal shift profiling[10-13], have revolutionized our understanding of drug activities, mapping *in vivo* drug targets with spatial and cellular resolution remains challenging. This shortfall is even more pressing in light of the innovations in genomics and imaging techniques over the past decade that have enabled the characterization of tissue architecture at the single-cell level with spatial resolution[14-20]. This has led to a widening gap between our understanding of native biological systems and our ability to track *in vivo* drug actions within these systems, as the latter still primarily rely on low-resolution methods such as radioactive imaging. It is imperative that we develop methods to visualize *in situ* drug engagement with cellular resolution across tissue compartments and organ systems to better understand *in vivo* drug actions.

One promising avenue for imaging drug targets is fluorescence imaging, which has been widely used for visualizing endogenous biomolecules like DNA, mRNA, and proteins. However, directly imaging drug molecules conjugated with a fluorescent tag is often not suitable as a larger tag could distort drug activity and distribution *in vivo*. As an alternative approach, we recently developed a method to visualize drug molecules in tissue sections by combining tissue clearing with *in situ* click chemistry (CATCH)[21]. However, efforts to extend CATCH from thin sections to large, heterogeneous 3D tissue environments face significant challenges similar to those typically encountered by whole-mount immunostaining or *in situ* hybridization methods, such as the accumulation of probes at the tissue surface, uneven staining across the tissue depth, and insufficient labeling at the center of large samples[22-26].

Here, we develop new CATCH capacities to enable rapid and homogenous *in situ* click labeling in ultra-large 3D tissues at the scale of a whole mouse body. This new technology leverages the unique characteristics of click chemistry by introducing pre-reaction copper saturation (PRCS) and repeated iterations of reaction (RIR). The resulting volumetric CATCH (vCATCH) method, when combined with HYBRiD (hydrogel-based reinforcement of three-dimensional imaging solvent-cleared organs (DISCO)) clearing[27], is further highlighted by its marked simplicity as it only relies on easy and passive incubation steps to achieve whole-body labeling and imaging.

RESULTS

Establishing the principles for deep tissue click reactions

To achieve 3D click labeling, we turned to recent advances in whole-brain and whole-body immunostaining techniques[24,28-35]. As summarized by previous works[36-39], two main strategies have been used to achieve deep tissue antibody penetration: (1) enhancing diffusion of the probe (e.g., antibody) into the tissue; and (2) minimizing probe-target interactions (e.g., antibody-antigen binding) during the diffusion stage while maximizing reaction efficiency at the staining stage, such that the large difference in reaction rates between the two stages will prevent probe depletion at the tissue surface and facilitate homogeneous tissue labeling[23,33,34]. Biophysics studies have demonstrated that changing the pH, salt concentration, and other physicochemical parameters can modulate antibody-antigen binding kinetics by 4-400 fold[40,41]. We hypothesized that we could adopt a similar strategy to enable 3D click reactions. CATCH relies on copper-

catalyzed alkyne azide cycloaddition (CuAAC) to label target-bound drug molecules with fluorescent signals. As its name indicates, the kinetics of CuAAC strictly depend on the catalytic Cu(I)-ligand complex, but for ease of handling, a Cu(II) compound, typically $CuSO_4$, is used during the diffusion stage and then a reducing agent (e.g., sodium ascorbate) is added *in situ* to generate Cu(I) at the binding stage. Compared to uncatalyzed conditions, the generation of catalytic Cu(I) can lower the energy barrier by 14.9-18.4 kcal/mol, or an equivalent of 7-8 orders of magnitude increase favoring the cycloaddition that attaches the fluorescent probe to the drug *in situ*[42]. Thus, by temporarily preventing the generation of Cu(I) from Cu(II) through withholding the reducing agent sodium ascorbate, in principle, we could modulate the probe-target reaction by 10^{7-8} fold between the diffusion and binding stages, which could improve the penetration depth of CATCH in large tissues.

For method development, we used the covalent monoamine oxidase (MAO) inhibitor pargyline, whose alkyne probe pargyline-yne has previously been characterized by activity-based protein profiling (ABPP) and 2D-CATCH studies (Figure S1A)[21,43]. Although CATCH has demonstrated homogeneous click labeling of N_3-dye in 500 μm tissues[21], when tested in mouse hemispheres, even with the aforementioned catalyst withholding strategy, only the surface of the mouse brain was labeled, a depth of 0.4 mm (Figure 1A). First, we used mouse brains treated with the fatty acid amide hydrolase (FAAH) inhibitor PF7845-yne (Figure S1A), another CATCH probe we previously established, to determine whether other CATCH components might have trouble diffusing through the tissue[21,44]. We removed individual reagents from the diffusion step and evaluated the resulting labeling depth. For instance, eliminating the N_3-dye, the largest molecular weight component, in the diffusion step did not affect labeling depth, suggesting N_3-dye diffusion is not a limiting factor (Figure S1B and S1C). By contrast, removing $CuSO_4$ or ligand strongly reduced labeling depth in these conditions, suggesting that the catalyst is still likely the diffusion bottleneck (Figure S1B and S1C).

Cu is well-known to bind multiple amino acid side chains (i.e., cysteine and histidine)[45-48]. We therefore hypothesized that the ubiquitous copper binding sites could consume free Cu(II) as it diffuses into the sample, resulting in insufficient catalyst conversion in deeper tissues (Figure 1B). Unlike typical staining in which increasing dye or antibody concentrations tends to result in nonspecific labeling and high background, high Cu(II) alone, as a catalytic precursor, should not lead to nonspecific labeling. Based on this theoretical prediction, we reasoned that excessive Cu(II) could be used to pre-saturate potential copper binding sites (therefore “blocking” them) to boost catalytic activity in deeper tissues. Importantly, this strategy should not increase nonspecific labeling or lead to high background. Indeed, we observed that incorporating a 10x Cu excess pre-reaction copper saturation (PRCS) step increased the reaction depth to 1 mm while maintaining the signal-to-noise ratio after a single one-hour reaction (Figure 1A-1C).

We next sought to modify CATCH to reach targets in tissues deeper than 1 mm. Although increasing reaction time could potentially increase labeling depth, prolonged reactions would deplete the reducing agent in the buffer, which could eventually lead to reactive oxygen species (ROS) build-up and side reactions[49-51]. Instead, we refreshed the click reaction cocktail every hour, a procedure we termed repeated iterations of reactions (RIR). In practice, PRCS plus two rounds of RIR resulted in full-depth, homogenous CATCH labeling across the mouse hemisphere (Figure 1A-1C, Supplementary Video 1). We term this approach volumetric CATCH (vCATCH).

132 **vCATCH quantitatively profiles brain-wide targets of Pargyline**

133 After achieving brain-wide labeling, we employed vCATCH to unbiasedly map drug targets of
134 pargyline. After intraperitoneal (i.p.) injection of pargyline-yne (10 mg/kg) or vehicle (non-drug
135 treated) in wild-type mice, mouse hemispheres were harvested and cleared by HYBRiD.
136 Hemispheres then underwent one day of PRCS and two rounds of RIR before imaging with
137 lightsheet fluorescence microscopy (Figure 1D). Importantly, vCATCH allowed the use of high-
138 throughput, paralleled passive processing to generate cohort-scale pargyline-labeled brains with
139 marked reproducibility, critical for performing biologically meaningful analysis of its cellular
140 targets across the whole brain (Figure 1E-1H, S1D, and S1E).

141 First, we manually verified pargyline probe binding in the brain based on previously reported
142 regional targets[21]. These regions included distinct cellular structures in the pons and
143 hypothalamus (Figure 1H and S1E). In addition, we found pargyline-yne-enriched cells in the
144 choroid plexus (in the ventricle) and the medulla (Figure 1H and S1E). We also observed
145 additional neuron-like structures in the midbrain (Figure S1E). These findings demonstrated that
146 vCATCH maintained high fidelity in large tissue volumes and across the whole brain.

147 The throughput and reproducibility of vCATCH across cohort-scale samples also allowed
148 automatic and unbiased quantification of drug targets beyond visual inspection. We applied a
149 recently developed AI-based Cartography of Ensembles (ACE) pipeline to analyze these datasets
150 (Figure 2A-2C, Supplementary Table 1)[52,53]. After registering the 3D volumes onto the Allen
151 Brain Atlas (ABA)[54] (Figure S2A), we first quantified the fluorescence intensity (indicating drug
152 binding abundance) across all brain regions (Figure 2B). Intensity quantifications revealed high
153 drug abundance in the pons, thalamus, and midbrain (summarized in Figure 2D and S2B), for
154 example, in the locus coeruleus (LC) and nucleus accumbens (ACB) (Figure 2D).

155 Leveraging the cellular resolution imaging provided by vCATCH, we next sought to unbiasedly
156 quantify the cell targets of pargyline. Empowered by a large training dataset and AI-based
157 segmentation algorithms, the ACE pipeline was used to identify brain-wide pargyline-yne-
158 positive cells (Figure 2C, S2C, and S2D). After segmentation, the cell density patterns generally
159 agreed with fluorescence intensity profiles. Since pargyline targets both MAO-A and MAO-B
160 with similar affinities[43], we performed MAO-A and MAO-B immunofluorescence and confirmed
161 that pargyline-yne-targeted cells overlap with either or both MAO-A/B protein expression,
162 consistent with the known affinity of pargyline on these two targets (Figure S2E)[43].

163 Interestingly, unbiased ACE analysis also revealed unexpected differences between fluorescence
164 intensity and cell counts. For example, the ACB, bed nuclei of the stria terminals (BST), and the
165 medial group of the dorsal thalamus (MED), showed extensive drug intensity, but almost no
166 neuronal structures were detected in these areas, indicating drug binding may be associated with
167 non-soma structures (Figure S1E, 2D, and 2E). Conversely, MAO-B positive drug-bound cells
168 were identified in the dorsal raphe (DR) and the anterior tegmental nucleus (AT) of the pons
169 (Figure S1E, 2D, 2E, and S2E) despite the lack of overall fluorescence intensity increase,
170 suggesting sparse neuronal populations were targeted by pargyline in these regions.

171 Taken together, by using a pargyline probe as a proof-of-concept, we demonstrated that vCATCH
172 is compatible with clearing methods and high-throughput computational pipelines to unbiasedly
173 quantify regional enrichment and cellular targets of covalent drugs in the mouse brain, which
174 was not possible with traditional methods.

175 **vCATCH profiles whole-body targets of covalent cancer drugs**

176 We next sought to expand vCATCH target mapping to whole animals across all organ systems.
177 We selected two widely used cancer drugs for this study: afatinib (Gilotrif®) and ibrutinib
178 (Imbruvica®), both covalent targeted kinase inhibitors (TKIs)[55,56]. Since their landmark approval
179 in 2013, the epidermal growth factor receptor (EGFR) inhibitor afatinib and Bruton's tyrosine
180 kinase (BTK) inhibitor ibrutinib, respectively, have transformed the clinical landscape of non-
181 small cell lung cancer (NSCLC)[57,58] and B cell malignancies[59-61]. Despite their popularity,
182 however, there are several well-documented side effects of TKIs that are poorly understood. For
183 example, ibrutinib is associated with cardiovascular and bleeding risks[62,63]. Although many
184 studies have been conducted to understand the protein targets (or off-targets) of ibrutinib[64-68], the
185 *in vivo* tissue(s) or cell types responsible for such toxicities remain elusive. The ability to
186 unbiasedly profile TKI targets *in vivo* at cellular resolution could provide crucial insight to
187 bridge this gap.

188 We injected previously established clickable probes of ibrutinib-yne (10 mg/kg, i.p.) and
189 afatinib-yne (10 mg/kg, i.p.) in wild-type mice (Figure S3A)[69]. These probes largely retain the
190 pharmacokinetics and tissue distribution of the parent compounds (Figure S3B and S3C). We
191 established a vCATCH protocol with 4-day PRCS and 5 rounds of RIR to homogenously label a
192 whole HYBRiD-cleared, one-week-old mouse with a total volume of more than 38x18x12mm
193 (Figure 3A-3D). Labeling specificity was again confirmed by controlling for each vCATCH
194 component in the lung or the spleen (canonical EGFR+ or BTK+ tissue, respectively, Figure
195 S3D-S3G).

196 We then performed whole-body lightsheet imaging of these 1-week-old mouse bodies (Figure
197 3B-3H, S3H, S3J-S3M) and visualized them through virtual reality (VR) (Supplementary Video
198 2 and 3)[70]. The performance of vCATCH in young mice motivated us to expand its capacity to
199 adult bodies. Enhanced by 7-day PRCS and 8 rounds of RIR (Figure 3A), we labeled ibrutinib-
200 yne in an adult mouse with a total volume of 70x30x20 mm. Although this whole volume
201 exceeded the field of view (FOV) of most commercial lightsheet systems, we were able to focus
202 on the center of the torso (37x30x8 mm, Figure 3I) and examined drug distribution of major
203 organs (Figure 3J-3M, and S3I).

204 Globally, the binding of both TKIs was highly abundant in the liver and the gastrointestinal tract
205 (Figure 3F, 3K, S3K and S4). In the upper chest, ibrutinib showed elevated heart binding
206 compared to the lung, whereas the opposite enrichment was observed with afatinib (Figure 4A,
207 4F and 4K). These findings are consistent with the general distributions of these two drugs based
208 on established autoradiography data from the Food and Drug Administration[71,72].

209 The resolution of vCATCH further allowed us to examine intra-organ drug distribution in detail.
210 In several organs, afatinib and ibrutinib displayed similar intra-organ distributions; for example,
211 both drugs were selectively enriched in the villus in the small intestine (Figure S4). Higher-
212 magnification confocal imaging further revealed detailed drug-bound structures across organs
213 (Figure 5A-5F). For example, both drugs strongly bound to circular structures in the bone
214 (Figure 5A and 5D), which were also observed in the spleen (Figure S4). Subsequent lectin
215 staining identified these structures as vasculatures (Figure S5A and S5B). Considering that BTK
216 expression is generally absent in blood vessels[73], we suspect the vasculature associated binding
217 may be implicated in the off-target toxicity associated with ibrutinib[62,63].

In other organs, we observed distinct target distributions between these two drugs. For example, robust tissue enrichments in the inner stomach lining and along the nasal tract were associated with ibrutinib but not afatinib (Figure S4A and S4B). Furthermore, we discovered widely spread afatinib targets in the lung, whereas pulmonary ibrutinib labeling was restricted along the bronchi (Figure 4B, 4C, 4G, 4H, 4L, and 4M).

Interestingly, although both drugs were bound to the kidney, they displayed different intra-organ patterns (Figure S4). Afatinib was associated with glomeruli in the cortex and near the cortex-medulla interface, whereas ibrutinib was more localized to cortical tubular-like structures (Figure 5B and 5E). Similarly, our global organ-level imaging (Figure 4D, 4I, and 4N) showed that both TKIs were enriched in the liver, in agreement with the literature[71,72]. However, higher resolution vCATCH revealed differences in their intra-organ distribution: afatinib showed crown-like signals throughout the hepatic tissue, whereas ibrutinib was associated with sparsely scattered individual cells, as demonstrated by both lightsheet (Figure 4E, 4J, and 4O) and confocal imaging (Figure 5C and 5F).

Multiplexed molecular characterizations of drug-enriched cellular structures

Guided by the drug distribution patterns, we next sought to molecularly characterize drug-targeted cells. We first focused on afatinib binding in the lung and ibrutinib binding in the spleen based on their canonical "on-target" engagements[73]. As expected[69], afatinib-yne and ibrutinib-yne signals were primarily on EGFR+ and BTK+ cells, respectively, as determined by immunostaining (Figure 5G and 5H). Importantly, pretreating the animals with the parent compound of each probe robustly reduced probe labeling (Figure 5G-5J), further confirming the specificity of these probes.

In the liver, we observed enriched yet distinct binding patterns of afatinib-yne and ibrutinib-yne (Figure 5C and 5F). We next performed molecular analysis to determine the targeted cell types of each probe. First, consistent with high EGFR expression in the hepatocytes[73], we found that the majority (59.17±10.91%) of afatinib-bound cells were hepatocytes, followed by small fractions of macrophages (F4/80+) and T cells (CD3e+) (Figure 5K-5M, and S5C). By contrast, only a small fraction (13.95±1.32%) of ibrutinib-bound cells were hepatocytes, while a larger proportion (39.53±4.42%) of these cells were F4/80+ macrophages (Figure 5N-5P), consistent with known BTK expression in liver macrophages[73]. Interestingly, the largest fraction (52.78±3.25%) of ibrutinib-bound cells were CD3e+ T cells despite their low BTK expression (Figure 5O and S5C-E)[73], suggesting non-BTK engagement could be involved (see Discussion).

Beyond the liver, we were also able to identify and quantify afatinib-enriched immune cell populations in other tissues such as the lung (Figure S5F-S5H). In summary, our vCATCH data revealed that the two TKIs are enriched in distinct cell types within individual tissues and organs, highlighting vCATCH's capacity to profile drug targets across global, organ, tissue, and cellular scales.

DISCUSSION

Covalent TKIs have reentered the stage for cancer treatment and broadened the horizon for the druggable space as demonstrated by the recent developments of mutant selective EGFR inhibitor osimertinib, and KRAS G12C inhibitors sotorasib and adagarasib[55]. However, despite the

261 reignited enthusiasm, the concern for toxicity (for example, cardiotoxicity and bleeding for
262 ibrutinib) calls for continuous innovations in characterizing their *in vivo* targets to guide future
263 covalent drug development.

264 Here, by treating samples with excessive copper (PRCS) and performing multiple rounds of click
265 reactions (RIR), we established a new method, vCATCH, which enabled robust covalent TKI
266 mapping across the whole mouse body. This method only requires simple passive incubations
267 and therefore offers reliability, reproducibility, and high throughput for cohort-scale biological
268 and pharmacological analyses. Using existing pharmacokinetic data from the Food and Drug
269 Administration (FDA) as a reference, vCATCH confirmed organ-level drug distribution.
270 Critically, vCATCH enabled us to identify drug engagement with intra-organ cellular resolution
271 that is typically inaccessible through conventional methods. The capacity to resolve drug
272 engagement across molecularly defined cell populations, tissue architectures, and organ systems,
273 once combined with single-cell and spatial omics tools, presents transformative opportunities for
274 spatially defined, cell-type-specific drug action characterization.

275 Our work so far has focused on wild-type mice for method development. By examining drug
276 binding in healthy mice, we uncovered patterns potentially associated with off-target engagement
277 and toxicities. For example, ibrutinib is well known to be associated with cardiac toxicity such as
278 atrial fibrillation (AF), but the mechanism behind this association remains incompletely
279 understood[64-67]. Although animal studies suggested AF induction would likely require chronic
280 administration[66], our study revealed clear ibrutinib enrichment in the heart after a single
281 injection, suggesting an intrinsic enrichment of ibrutinib for the cardiovascular system. It would
282 be of great interest to further examine ibrutinib engagement in AF models to better understand its
283 cardiotoxicity mechanism. In addition to AF, bleeding is another major ibrutinib risk factor[62,63].
284 Despite low BTK expression in endothelial cells[73], we observed ibrutinib engagement in the
285 vasculature, a finding that could have implications for ibrutinib-associated hypertension and help
286 guide subsequent molecular identification work to further characterize unique ibrutinib targets in
287 endothelial cells[75].

288 Moreover, we observed ibrutinib binding in T cells that normally do not express BTK. This
289 binding suggested non-BTK targets of ibrutinib at the dose we used in our studies. Indeed,
290 previous ABPP studies in Ramos cells have identified human epidermal growth factor receptor 2
291 (HER2)[69] as an ibrutinib target. *In vitro* kinase activity profiling also identified interleukin-2
292 inducible T-cell kinase (ITK) and Janus kinase 3 (JAK3) with nM affinity to ibrutinib[68]. All of
293 these non-BTK affinities could contribute to our observed T cell binding.

294 On the technology side, vCATCH represents a new strategy to use biorthogonal click chemistry
295 to label large tissues, in contrast to most mainstream labeling methods (e.g., immunostaining,
296 DNA/RNA hybridization, etc) that primarily rely on biological affinities, such as antibody-
297 antigen, biotin-streptavidin, and complementary DNA/RNA interactions. Click chemistry allows
298 us to easily control labeling kinetics by simple buffer exchanges, achieving uniform probe
299 penetration in ultra-large tissue without delicate procedures or apparatus. The covalent click
300 chemistry linkage also means that the same sample can withstand harsh and prolonged
301 processing and imaging operations, opening numerous possibilities to multiplex vCATCH with
302 other spatial omics methods.

303 Finally, it is a major challenge in whole-mount tissue staining to balance the high probe
304 concentration (such as antibody) required for tissue penetration and its associated background

resulting from the nonspecific interactions between the probe and endogenous biomolecules. In this regard, the biorthogonal nature of click chemistry could better tolerate a wide range of labeling conditions without increasing noise. Currently, click chemistry-based imaging studies are primarily associated with examining transcription/translation[77,78]. By demonstrating vCATCH's capacity to map covalent drug binding across the entire mouse body, we propose that similar principles can be applied in ultra-large 3D tissues to visualize substrates including but not limited to protein[79], nucleic acid[80], glycan[81], lipid[82], and drug molecules[21]. For example, a recent study (Click3D) has demonstrated that the original CATCH or similar strategies can label endogenous RNA and dyes in the mouse brain and tumor[83], suggesting such approaches could be adopted in future biomedical studies, although it was limited to small, individual organs.

LIMITATIONS OF THE STUDY

Focusing on method development, our current study used healthy wild-type mice, in which the engagement of TKIs could differ from tumor-bearing animals. Given the robustness and simplicity of the vCATCH pipeline, however, we believe other researchers with oncology expertise could readily apply vCATCH in various cancer models. We also note that due to the size limit of the current lightsheet microscopes, our imaging scope is limited to the center of adult mouse torsos. We foresee that the challenge can be addressed with emerging hardware and reconstruction pipelines[31,84,85]. Moreover, all clickable TKI probes used in this study have been rigorously validated by published medicinal chemistry and chemoproteomics studies[69]. However, we acknowledge that generating alkyne derivatives with similar absorption, distribution, metabolism, and excretion (ADME) properties of the original drugs requires dedicated efforts. We note that our ibrutinib-yne probe has a higher liver distribution than the parent drug, despite the latter being known to be enriched in the liver based on the FDA[72]. This difference could confound our interpretations of ibrutinib-bound immune cells (Figure 5). Lastly, as CATCH readout can potentially reflect both on- and off-target binding and metabolite intermediates (i.e., glutathione conjugation for cysteine-targeting drugs), it is important to note that the design of future CATCH probes for other drugs must be verified by similar PK and target identification approaches; although it is becoming common to generate and characterize clickable alkyne analogs during the development of new covalent inhibitors.

RESOURCE AVAILABILITY

Lead Contact

Further information and requests for resources and reagents should be directed to and will be fulfilled by the lead contact, Li Ye (liye@scripps.edu)

Materials availability

All unique/stable reagents generated in this study are available from the lead contact with a completed materials transfer agreement.

Data and code availability

All data are available in the main text or the supplementary materials. Any additional information required to reanalyze the data reported in this paper is available from the lead contact upon request. Relevant code for the study is available from https://github.com/yelabscripps/vCATCH.

ACKNOWLEDGMENTS

We thank all members of the Ye lab and the Dorris Neuroscience Center for their support and feedback. We thank Barry Sharpless for suggestions. This work was supported by NCI IMAT program (CA281918 to L.Y. and B.F.C), NIH Director's New Innovator Award (DK128800 to L.Y.), and NIDA (DA059393 to L.Y.). L.Y. was also supported by the HHMI, NIDDK, NIMH/BRAIN, Chan Zuckerberg Initiative, and the Dana, Whitehall, Baxter, and Abide-Vividion Foundations. J.J.M received funding from the NIH (R01HL141466, R01HL155990, R01HL156021, P01HL141084). Z.P. and H.S. were supported by the Dorris Scholar Award. L.H.S is supported by an NIH Medical Scientist Training Grant T32GM007198-49. M.D.M.-G. was supported by Stanford Wu Tsai Human Performance Alliance. P.W. is supported by the NIH (R35GM139643).

AUTHOR CONTRIBUTIONS

L.Y., Z.P. conceived the study. L.Y., Z.P., V.H.L., P.W., J.J.M., J.Z.L., M.G., and B.F.C. designed the experiments. Z.P., V.H.L., C.C.W., C.G., L.H.S., M.Y., A.S., and S.X. performed the experiments and analyzed the data. A.A., A.R., H.S., and M.G. performed the ACE analysis. Z.P., V.H.L., and M.D.M.-G. performed the PK study. Z.P., V.H.L., and C.R. performed the parental drug blocking study. L.Y. and B.F.C. acquired funding. L.Y. supervised the study. L.Y., Z.P., V.H.L., and C.C.W. wrote the manuscript with input from all authors. All authors reviewed and provided feedback on the manuscript.

DECLARATION OF INTERESTS

The design, steps, and applications of vCATCH are covered in pending patent application material from The Scripps Research Institute.

372 **FIGURE LEGENDS:**

373 **Figure 1. Establishing the principles for deep tissue click reactions**
374 (A) Brain-wide characterization of click labeling in pargyline-yne-treated hemispheres (10
375 mg/kg, 1 h, i.p.). Pre-reaction copper saturation (PRCS) and repeated iterations of reactions
376 (RIR, 1 hour per iteration) enhanced labeling depth and generated homogeneous click labeling
377 across the whole hemisphere.
378 (B) Schematics of copper competition in tissue. Copper binding sites could chelate copper
379 and limit the available free copper for CuAAC catalyst conversion, thereby impairing click
380 labeling efficiency deep in tissues.
381 (C) Quantification of click labeling depth along the marked lines in Figure 1A. Four
382 hemispheres in each condition.
383 (D) Representative 3D rendering of vehicle and pargyline-yne treated hemispheres.
384 (E) 3D rendering of pargyline-yne treated hemispheres showing the total imaging volume.
385 (F) Schematics of imaging depth shown in Figure 1G, highlighting changes in different brain
386 regions covered.
387 (G) Sagittal 2D views of pargyline-yne treated hemispheres at imaging depth Z=1.5 mm and
388 3.0 mm as indicated in Figure 1F.
389 (H) Zoomed-in views showing pargyline-yne enriched neurons and brain regions across the
390 hemisphere.
391 Data are plotted as mean±SEM. Scale bars: 1000 μm (A); 2000 μm (D and G); 100 μm (H)

392 **Figure 2. ACE analysis of pargyline-yne targets across the hemisphere.**
393 (A) Schematics of the ACE analysis pipeline for brain wide pargyline-yne (10 mg/kg, 1 h,
394 i.p.) target identification.
395 (B) Representative regional drug intensity quantification in atlas space. White boundary
396 indicates brain regions by Allen Brain Atlas (ABA). The LC showed the highest overall
397 labeling intensity in pargyline-yne hemispheres. Raw intensity values indicated by scale bar.
398 (C) Representative segmented neurons in atlas space. Known pargyline-yne-bound neurons in
399 the pons and hypothalamus were used as positive controls. Additional neuronal structures (i.e.
400 in the medulla) were identified. The scale bar indicates raw segmented neuron density in each
401 10x10x10 μm voxel.
402 (D-E) Heatmap of normalized pargyline-yne labeling intensity (D) and normalized pargyline-
403 yne positive neuron density (E). A total of 5 pargyline-yne-treated mice (rows) and 184 brain
404 regions (columns) were included for analysis. For individual mice, intensity and density
405 values were normalized by the average intensity and density of all the regions from each
406 mouse. Purple labels indicate regions with only elevated intensity. Blue labels indicate
407 regions with only elevated neuronal density. Red labels indicate regions with shared elevated
408 intensity and neuronal density. Barrington's nucleus (B*) was later found to be a false
409 positive (See Figure S2F). The full dataset and acronyms can be found in Supplementary
410 Table 1. EPI, epithalamus; PMD, dorsal premammillary nucleus; PMV, ventral
411 premammillary nucleus; AT, anterior tegmental nucleus; SLC, subceruleus nucleus; SLD,
412 sublaterodorsal nucleus; AMB, nucleus ambiguus; VS, ventricular system.

413 **Figure 3. vCATCH reveals whole-body TKI distribution with high spatial resolution.**
414 (A) Workflow of vCATCH whole-body labeling with estimated time of each step.
415 (B) Schematic of imaging depth.

(C) Coronal (x-y) views of vCATCH whole-body labeling in ibrutinib-yne (10 mg/kg, 1 h, i.p.) treated juvenile mouse across different z-depths.
(D) Schematic of lightsheet acquisition FOV, represented by red dotted box, for juvenile whole body.
(E) Representative ibrutinib-yne distribution overviews in a juvenile mouse with digital plane slicing in 3D volume.
(F-H) Coronal (F), sagittal (G), and transverse (H) views of a juvenile mouse as shown in Figure 3E.
(I) Schematic of lightsheet acquisition FOV, represented by a red dotted box, for adult mouse torso.
(J) Representative ibrutinib-yne distribution overview in an adult mouse torso with digital plane slicing in 3D volume image.
(K-M) Coronal (K), sagittal (L), and transverse (M) views of adult mouse as shown in Figure 3J.
Dashed lines indicate body boundary. Scale bars: 4000 µm (C, E, F, J, K); 2000 µm (G, H, L, M).

Figure 4. vCATCH reveals intra-organ TKI distribution
(A-E) Afatinib-yne binding in the upper chest (A), lung (B and C), and liver (D and E) of juvenile mice.
(F-J) Ibrutinib-yne binding in the upper chest (F), lung (G and H), and liver (I and J) of juvenile mice.
(K-O) Ibrutinib-yne binding in adult mice. Figures showing the upper chest (K), lung (L and M), and liver (N and O).
Arrows indicate drug-enriched structures. Dashed lines indicate tissue boundary. Scale bars: 1000 µm (A, B, F, G); 500 µm (C, D, H, I, M, O); 100 µm (E, J); 2000 µm (K, L, N).

Figure 5. Cell type characterization of TKI engagement in drug-enriched tissues.
(A-F) Afatinib-yne (A-C) and ibrutinib-yne (D-F) characterizations in the bone (A, D), kidney (B, E), and liver (C, F).
(G) Afatinib pretreatment (25 mg/kg, 1 h, i.p.) in the lung co-stained with EGFR.
(H) Ibrutinib pretreatment (25 mg/kg, 1 h, i.p.) in the spleen co-stained with BTK.
(I-J) Quantification of afatinib-yne labeling intensity of EGFR-positive pixels in the lung (I) and ibrutinib labeling intensity of BTK-positive pixels in the spleen (J). n = 4 mice for each condition. One-way ANOVA with Tukey's multiple comparisons test. p-values plotted in the graph.
(K) Representative images of afatinib-yne+ hepatocytes (top row) and afatinib-yne+ macrophages (F4/80+, bottom row).
(L-M) Afatinib-yne positive cell type (L) and cell type specific intensity (M) quantifications. n=4 biological replicates, 4-6 FOV were acquired for each mouse.
(N) Representative images of ibrutinib-yne+ hepatocytes (top row) and ibrutinib-yne+ macrophages (F4/80+, bottom row).
(O-P) Ibrutinib-yne positive cell type (O) and cell type specific intensity (P) quantifications. n=4 biological replicates, 4-6 FOV were acquired for each mouse.
All values are shown as mean ± SEM. Dashed lines represent the cell boundary. Detailed cell type quantification is in Supplementary Table 1. Scale bars: 200 µm (A, C, global view; B, E, zoomed-in view; G, H); 20 µm (A, C, zoomed-in view); 1000 µm (B, E, global view); 500 µm (C, F, global view); 50 µm (C, F, zoomed-in view); 10 µm (K, N).

Figure S1. vCATCH development, related to Figure 1.

(A) Chemical structure of the monoamine oxidase A/B (MAO A/B) inhibitor pargyline, fatty acid amide hydrolase (FAAH) inhibitor PF7845, and their alkyne analogs used in the study. Both analogs have been verified in previous CATCH and ABPP studies.

(B) CATCH in 100-micron vehicle or PF7845-yne treated (1 mg/kg, 1 h, i.p.) brain sections. Individual components (Cu, ligand, N_3) were removed during the click reaction incubation. Representative images were taken at the primary somatosensory cortex (S1, imaging depth Z=10 and 50 microns).

(C) Quantification of CATCH intensity in Figure S1B. Six tissue sections (one field of view per section) were used for each condition. Intensity at Z=10 or 50 microns was measured and then normalized to the average vehicle labeling intensity at Z=10 or 50 microns, respectively. Paired t-test in each condition. P-values are plotted in the graph. n = 6 tissue sections for each condition.

(D) Transverse 2D views of hemispheres in Figure 1E.

(E) Coronal 2D views of hemispheres in Figure 1E. Zoomed-in views showing pargyline-yne enriched structures across the whole brain.

Statistics determined by two-tailed paired t-test in (C). Dashed lines indicate tissue boundary. Scale bars: 20 µm (B); 2000 µm (D); 1000 µm (E, coronal view); 100 µm (E, zoom-in view) ACB, nucleus accumbens; MED, medial group of the dorsal thalamus; PMV, ventral premammillary nucleus; DR, dorsal nucleus raphe; AT, anterior tegmental nucleus; LC, locus coeruleus.

Figure S2. ACE analysis and validation, related to Figure 2.

(A) Evaluation of ACE registration and warping algorithms. Lightsheet data were registered to the ABA using ACE. Left and right panels show data overlaid on labels for two subjects in each group. Segmentation maps from ACE were voxelized and warped to ABA 25-µm resolution. Panels show a randomly selected subject from the pargyline group.

(B) Atlas plot of the average intensity difference of vCATCH labeling intensity of vehicle vs. pargyline-yne treated samples. The greatest labeling intensity elevation is denoted in yellow.

(C) Atlas plot of the average segmented neuronal density (number of cells per mm^3) of vehicle vs. pargyline-yne treated samples. The greatest density elevation is denoted in yellow.

(D) Atlas plot of the average [-log(p-value)] of segmented neuronal density in vehicle vs. pargyline-yne treated samples. The greatest statistical significance is denoted in yellow.

(E) MAO-A and -B immunostaining in pargyline-yne positive regions.

(F) Histology validation of pargyline-yne binding in the LC. The boundary of LC and B is identified by NeuN and tyrosine hydroxylase (TH) staining using a published protocol[86]. Pargyline-yne binding is restricted in LC, suggesting that "B" was likely a false positive from ACE due to its small size.

Scale bars: 200 µm (E and F).

Figure S3: Whole body vCATCH visualization of TKI binding, related to Figure 3.

(A) Chemical structures of afatinib, ibrutinib, and their alkyne analogs.

(B) PK studies of plasma drug concentrations. Plasma samples taken 15, 30 and 60 min after drug injection (10 mg/kg). Two parental afatinib-60 min samples were excluded as outliers. n=4 mice for all time points except parental afatinib at 60 min (n = 2 mice).

(C) PK studies of tissue drug concentrations at 60 min post injection (10 mg/kg). n=4 mice for afatinib-yne, ibrutinib, and ibrutinib-yne; n=2 mice for afatinib.

(D-E) Click reaction specificity validation in afatinib-yne treated lung (D) and ibrutinib-yne treated spleen (E).
(F-G) Quantifications of click labeling intensity in afatinib-yne-treated lung (F) and ibrutinib-yne treated spleen (G). Intensity normalized to vehicle full click condition. Three independent tissues were used for quantification. Two-way ANOVA with Šidák multiple comparisons test.
(H) Representative 3D lightsheet image volume of whole-body drug distribution (10 mg/kg, 1h, i.p.) in juvenile vehicle, afatinib-yne, and ibrutinib-yne mice. D, dorsal; V, ventral; S, superior; I, inferior; R, right; L, left.
(I) Adult whole torso 3D overview of mice treated with vehicle and ibrutinib-yne (10 mg/kg, 1h, i.p.).
(J) Afatinib-yne distribution overviews with digital plane slicing in 3D volume image.
(K-M) Coronal (K), sagittal (L), and transverse (M) views of mice injected with afatinib-yne as shown in Figure S3J.
Data are plotted as mean ± SEM. Dashed lines indicate tissue boundary. Scale bars: 200 µm (D, E); 4000 µm (H, I, J, K); 2000 µm (L, M).

Figure S4: Organ level TKI binding, related to Figure 4.

(A) Representative organ views from afatinib-yne treated mice. Afatinib-yne enrichment was observed in small intestine villi, spleen central arterioles (orange arrows), and kidney cortex. No significant drug enrichment observed in the stomach lining or nasal tract. Scale bars: small intestine, kidney, stomach, and nasal tract, 500 µm; spleen, 250 µm.
(B) Representative organ views from ibrutinib-yne treated mice. Ibrutinib-yne enrichment was observed in small intestine villi, spleen central arterioles (green arrows), kidney, and inner stomach lining. Scale bars: kidney and stomach, 500 µm; small intestine and nasal tract, 300 µm; spleen, 200 µm.
(C) Representative organ views from ibrutinib-yne treated adult mice. Ibrutinib-yne enrichment was observed in small intestine villi, spleen central arterioles (green arrows), and kidney. Scale bars: small intestine, 1000 µm; spleen, 500 µm; kidney, 1500 µm kidney.

Figure S5: TKI positive cell type characterization, related to Figure 5.

(A-B) Lectin staining in bone (A) and spleen (B) sections after CATCH labeling. Representative images showing lectin overlaps TKI enriched labeling structures.
(C) High resolution afatinib-yne and ibrutinib T cell characterization in the liver. Representative images show CD3e+ cells that are afatinib- (left) and ibrutinib+ (right). Arrows indicate CD3e+ cells.
(D) Cell type characterizations of ibrutinib-yne positive liver T cells. Samples are co-stained for helper T cells (CD4) and cytotoxic T cells (CD8).
(E) Quantifications ibrutinib-yne positive T cell subtypes in the liver. n=4 biological replicates, 11-17 FOV were acquired for each mouse.
(F) Global characterization of afatinib-yne binding in the lung. Zoom-in views showing discrete afatinib-yne enriched structures scattered throughout the lung.
(G) High resolution afatinib-yne cell type characterization in the lung. Representative images showing afatinib-yne enriched F4/80 positive macrophages (top) and CD19 positive B cells (bottom).
(H) Cell type characterization of afatinib-yne enriched cells in the lung. n=4 biological replicates, 5-6 FOV were acquired for each mouse.

All values are shown as mean ± SEM. Detailed cell type quantification is in Supplementary Table 1. Scale bars: 20 µm (A and B); 10 µm (C, D, and G); 1000 µm (F, global view); 50 µm (F, zoomed-in view).

STAR METHODS

Key Resources Table

EXPERIMENTAL MODEL AND SUBJECT DETAILS

Mouse model

Mice were group-housed on a 12-hr light-dark cycle and fed a standard rodent chow diet. Both male and female mice were used for the study. Six to nine-week-old WT C57BL6J mice were used for vCATCH method development in 100-micron sections and hemispheres. One-week-old and eight-week-old WT C57BL6J mice were used for vCATCH in the whole mouse body. All experimental protocols were approved by the Scripps Research Institute Institutional Animal Care and Use Committee and were in accordance with the guidelines from the NIH.

Sample collection

Alkyne drugs were administered to mice in a vehicle of 10% DMSO and 2% Tween-80 in saline for i.p. injections at the indicated dose. 1 hour (for most direct labeling experiments) or 4 hour (for pretreatment test) after injections, mice were heavily anesthetized with isoflurane and then transcardially perfused with ice-cold PBS, followed by ice-cold 4% PFA solution. Mouse organs were carefully dissected and then post-fixed in 4% PFA solution overnight at 4℃. Tissues were washed with PBS. Mouse brains were embedded in 2% agarose and sectioned with a vibratome (Leica VT1000S) at 100-micron thickness. For hemispheres, brains were cut along the midline with a razor knife. Peripheral organs from one-week-old mice were dehydrated in 30% sucrose at 4℃ prior to sectioning. Samples were then carefully dried with a kimwipe and embedded in O.C.T. compound. After reaching equilibrium at -20℃, samples were cut at 100-micron thickness with a cryostat (Leica CM 1860). All obtained samples were stored in PBS with 0.02% sodium azide at 4℃ for further processing.

For mice used in whole-body drug distribution labeling, the skin was carefully removed immediately after perfusion, and the peritoneum was cut down the midline to facilitate clearing and click reactions. Mice were post-fixed in 4% PFA solution for two days at 4℃ followed by 7-day decalcification treatment in 10% EDTA/15% Imidazole at 4℃. Then, samples underwent decoloring treatment with 25% N, N, N’, N’-Tetrakis(2 Hydroxypropyl)ethylenediamine (Quadrol) in 1x PBS at 37°C with gentle agitation for 7 days. After PBS washes to remove Quadrol, mouse whole bodies were stored in PBS with 0.02% sodium azide at 4℃ for further processing.

For mice used in PK studies, after anesthesia, blood was collected via cardiac puncture and immediately stored in a heparin tube and placed on ice. Plasma was separated by centrifugation at 5,000 rpm for 5 min at 4°C. Next, 150 µL of a 2:1 mixture of acetonitrile/methanol was added to 50 µL of plasma. The mixture was then centrifuged at 15,000 rpm for 10 min at 4°C, and the supernatant was transferred to a liquid chromatography-mass spectrometry (LC-MS) vial. Tissue

592 samples were dissected out and weighed. Next, tissues were homogenized in water at 250 mg/ml
593 using a Homogenizer at 4°C. The mixture was then centrifuged at 15,000 rpm for 10 min at 4°C.
594 50 μL of the supernatant was then collected, and 150 μL of 2:1 mixture of acetonitrile/methanol
595 was added to the supernatant. The mixture was then centrifuged at 4°C at 15,000 rpm for 10 min,
596 and the supernatant was transferred to an LC-MS vial. To generate a standard curve, compounds
597 were dissolved in a 2:1:1 mixture of acetonitrile/methanol/water at 10, 1, 0.1, 0.01, 0.001 μM for
598 MS analysis.

599 **Tissue clearing**

600 *CLARITY*

601 100-micron sections were cleared with CLARITY as previously described[22,87]. Briefly, samples
602 were incubated in A1P4 hydrogel (1% acrylamide, 0.125% Bis, 4% PFA, 0.025% VA-044
603 initiator (w/v), in 1X PBS at 4°C for CLARITY embedding. After overnight incubation with
604 gentle agitation, samples were then degassed and polymerized at 37°C for 4 hours with gentle
605 agitation. Samples were removed from hydrogel and washed with 6% PBS-SDS (pH=7.0) at
606 37°C for two days. After clearing, samples were washed with PBST (pH=7.0 with 0.2% Triton-
607 X100, same for the following) three times (10 min each time) at RT to remove residue SDS.
608 Samples were briefly washed with PBS and then stored in PBS with 0.02% sodium azide at 4°C.

609 *HYBRiD*

610 Mouse hemispheres and bodies were cleared with HYBRiD as previously described[27]. In brief,
611 samples were dehydrated in an increasing THF/25% Quadrol gradient (50%, 70%, 80%, 100%,
612 100%; 1 hour per step for hemispheres, 3-12 hours per step for whole bodies), delipidated three
613 times in DCM (1 hour each for hemispheres, 3-12 hours each for whole bodies), and rehydrated
614 in a decreasing THF/25% Quadrol gradient (100%, 100%, 80%, 70%, 50%; 0.5 hour per step for
615 hemispheres, 1.5-6 hours per step for whole bodies). After clearing, samples were extensively
616 washed with PBS to remove residual organic solvent before hydrogel embedding. Samples were
617 equilibrated in A1P4 hydrogel (3 days for hemispheres, 7-10 days with one refreshment for
618 whole bodies) at 4°C on a shaker, then degassed and polymerized at 37°C for 4 hours with gentle
619 agitation. Thereafter, samples were passively cleared with LiOH Boric Buffer with 6% SDS
620 (pH=9) until transparent (1 week for hemispheres, 6-10 weeks for whole bodies). Samples were
621 extensively washed in PBST to remove residual SDS and then stored in PBS with 0.02% sodium
622 azide at 4°C.

623 **Click labeling in tissues**

624 *CATCH in 100-micron sections*

625 100-micron sections were labeled with an updated CATCH protocol. Unless otherwise noted,
626 sections were incubated in 10 mM $CuSO_4$ in H_2O at RT overnight. Sections were then transferred
627 to CATCH reaction buffer containing 5 μM AZDye 647-picolyl azide, 150 μM CuSO4, 300 μM
628 BTTP, 2.5 mM NaAsb, and 10% DMSO in 1X PBS. After 1 hour of reaction in the dark with
629 minor agitation, samples were washed with buffer containing 4 mM EDTA in PBST (PBST-
630 EDTA, same for the following) at RT for 3x10 min. Tissue samples were then stained with DAPI
631 (1:3000 dilution in PBST from 10 μM stock) for 15 mins at RT. Samples were then either used
632 for refractive index (RI) matching by RapiClear and confocal imaging or proceeded to further
633 immunolabeling for cell-type registration.

634 *vCATCH in hemispheres*

635 For hemisphere labeling, each hemisphere was first pre-incubated with 25 mL of 10 mM CuSO4
636 in H_2O for one day at RT for PRCS. Hemispheres were transferred to vCATCH incubation buffer
637 (5 μM AZDye 647-picolyl azide, 1 mM CuSO4, 2 mM BTTP, 10% DMSO in 1X PBS, 3 mL for
638 each hemisphere) for 1 day at RT. Hemispheres were then transferred to the newly prepared full
639 vCATCH reaction buffer (5 μM AZDye 647-picolyl azide, 1 mM CuSO4, 2 mM BTTP, 25 mM
640 NaAsb, 10% DMSO in 1X PBS, 3 mL for each hemisphere) for click labeling. The vCATCH
641 reaction buffer was refreshed every hour for two rounds of RIR. Hemispheres were washed with
642 PBST-EDTA at RT. The washing buffer was refreshed at the end of the day and then daily until it
643 became colorless. The hemispheres were then washed with PBST for 1 hour at RT. After
644 washing, hemispheres were cut into 100-micron coronal sections for labeling depth
645 characterizations. Alternatively, hemispheres were carefully dried with a Kimwipe and then
646 incubated in 3 mL EasyIndex for RI matching and lightsheet imaging.

647 *vCATCH in the whole mouse*

648 Cleared mouse bodies were placed in 500 mL per mouse of 10 mM $CuSO_4$ in H_2O with agitation
649 for 4-7 days at RT with daily buffer refreshes. After PRCS, whole-body samples were
650 individually incubated in 10-40 mL of vCATCH incubation buffer for 3-5 days on a shaker at RT
651 with daily buffer changes. Samples were then transferred to vCATCH reaction buffer (10-40 mL
652 each) to initiate the reaction. Five to eight successive rounds of 1-hour click reactions were
653 performed to thoroughly label the entire tissue depth. After click labeling, samples were washed
654 with PBST-EDTA with daily refreshments until the buffer was colorless. After an additional day
655 of PBST wash, mouse bodies were carefully dried with a Kimwipe and then thoroughly
656 immersed in 25-40 mL EasyIndex at 37°C for thorough RI matching in preparation for lightsheet
657 imaging.

658 **Immunostaining**

659 CATCH-labeled 100-micron sections were incubated with primary antibodies 1:200 diluted in
660 PBST overnight at 4°C. Samples were then washed with PBST 3 x 30 min at RT prior to
661 incubation with secondary antibodies diluted 1:600 in PBST. Samples were then incubated with
662 secondary antibodies 1:600 diluted in PBST. Samples were incubated with secondary antibodies
663 overnight and then washed with PBST 3 x 30 min at RT.

664 **Confocal microscopy**

665 100-micron samples were mounted with RapiClear for RI matching and imaged with an
666 Olympus FV3000 confocal microscope. To characterize CATCH labeling depth in 100-micron
667 sections, samples were imaged at the primary somatosensory cortex layer V with a 10X, 0.6 NA,
668 water immersion objective (XLUMPlanFI, Olympus) at 0.414 micron/pixel resolution and a step
669 size of 10 microns. To examine hemisphere labeling depth and global drug distribution within
670 individual organs, samples were imaged with a 10X, 0.6 NA, water immersion objective
671 (XLUMPlanFI, Olympus) at 2.49 microns/pixel resolution and a step size of 10 microns. For cell
672 type characterizations, samples were imaged at the top surface with a 40X, 1.25 NA, silicone oil
673 objective (UPlanSApo, Olympus) at 0.094 micron/pixel resolution and a step size of 3 microns.
674 All confocal data was saved in TIFF format for further analysis.

675 **Lightsheet microscopy**

676 Whole hemisphere/body samples were imaged using a lightsheet microscope from LifeCanvas
677 Technologies. RI-matched whole hemisphere and body samples were mounted in 1%
678 agarose/Easy Index for imaging. Lightsheet imaging was performed in a SmartSPIM chamber
679 with Easy Index matched immersion oil (RI=1.52). A 3.6x objective was used with 0.28 NA,
680 1.8μm/1.8μm/2μm *xyz* voxel size. Imaging was performed by illuminating samples along the
681 bilateral plane of symmetry. Lightsheet raw data was then destriped, stitched, and saved as TIFF
682 format for further conversion.

683 **Image processing and analysis**

684 *Hemisphere labeling depth characterization*

685 Hemispheres were sectioned coronally as 100 micron sections and imaged to characterize
686 vCATCH labeling depth. Images were first processed as maximum intensity projection. A
687 rectangular area (805 x 50 pixels, 2001.17 x 136.73 microns) was drawn from the cortical outer
688 layer inwards (from tissue surface to tissue center) as indicated in Figure 1A. The signal profile
689 was plotted using the 'Plot Profile' function in ImageJ as reported[27,88,89]. The fluorescence signal
690 profile was then normalized by the intensity value at the start of the line.

691 *Thin section labeling depth characterization*

692 CATCH labeling intensity across the 100-micron section was quantified as previously
693 reported[21,27,88]. Briefly, a 150 x 150 pixel (62.1 x 62.1 micron) ROI surrounding a labeled neuron
694 was generated at z = 10 μm and 50 μm at cortex layer V, and an auto threshold was applied to
695 measure the mean drug-positive pixel intensity as I_{signal}. The mean intensity of the remaining
696 pixels was used $I_{background}$. The mean labeling intensity was defined as $I_{labeling}=I_{signal}-I_{background}$.

697 *Cell type-specific characterization*

698 CD3e, F4/80, CD4, CD8, and CD19 positive cells were characterized by immune staining.
699 Hepatocytes were identified based on their large size (20-30 microns), round/oval-shaped
700 nucleus, and hexagonal morphology by well-trained experts. To minimize bias, individual fields
701 of view (FOV) were first acquired based on the DAPI and the immunostaining channel without
702 knowledge of the CATCH/drug channel (with the exception of CD3e+ibrutinib+ cells, where the
703 CD4 and CD8 channel were kept blind during imaging acquisition) to assign cell types. The
704 CATCH positivity was post-hoc assigned to individual cells after their cell types have been
705 determined, followed by overlapping quantifications. For intensity characterizations, individual
706 cells were selected along the boundary and cropped out for quantification. A threshold was
707 applied in the drug channel to analyze CATCH labeling intensity in individual cells of interest.
708 The full dataset of each cell population can be found in Supplementary Table 1.

709 *Global drug intensity characterization*

710 To measure global drug intensity across intact thin tissue sections, confocal images were first
711 processed as maximum intensity projections. A threshold was then applied in the counterstain
712 channel (DAPI or target immunostaining) to cover the whole tissue or target positive pixels. The
713 threshold area was selected as tissue containing pixels. The average drug channel intensity in the
714 selected pixels was then quantified as global drug intensity.

715 *Volumetric drug binding visualization*

Lightsheet imaged hemispheres and whole body images were converted into Imaris files and visualized via Imaris 10.2.0. The hemisphere drug labeling video was generated by Imaris. For VR-based whole-body drug visualization, data was converted by syGlass, and videos were made with a Meta Quest 3 glass. For hemisphere coronal and transverse views, TIFF files were imported as image sequences and then resliced by Fiji ImageJ. For drug distribution visualization across organs, TIFF files were imported as image sequences and sampled at 100-micron step size. Individual organ of interest was then cropped out for visualization.

Automated Brain-wide Cell Mapping & Signal Intensity Calculation.

We employed an AI-based Cartography of Ensembles (ACE) pipeline to generate whole-brain segmentation maps of pargyline-yne+ cells[53]. ACE is an open-source 3D deep learning pipeline (available through the MIRACL platform[90]; https://miracl.readthedocs.io/) to map local cell activations using tera-voxel size light sheet microscopy datasets. Given the significant differences in morphological features between pargyline-yne+ cells and cFos+ cells (which the ACE models were originally trained on), we first fine-tuned the ACE vision transformer (ViT) model. For fine-tuning, we randomly selected 225 image patches of 963 voxels each (0.17x0.17x0.19 mm^3) from two subjects in the dataset and generated ground truth using the Labkit annotator[91] in ImageJ/Fiji software[92]. We fine-tuned the ViT model on half of these patches and used the other half for evaluation. The model was fine-tuned for 200 epochs using the Adam optimizer[93] with an initial learning rate of 0.0001 and an equally weighted Dice-Cross Entropy loss function. To account for artifacts in the dataset, the cross-entropy calculation for "background" voxels was weighted 2× higher than for voxels annotated as pargyline-yne+ cells. The best model, which achieved an average Dice score of 0.7 on the validation dataset, was used to generate segmentation maps for the entire dataset. Subsequently, a shape filter was applied to the segmentation maps to eliminate false positives such as vasculature traces in cortical regions using the shape filter plugin in ImageJ/Fiji[94]. To distinguish individual cells, a connected component analysis was applied to the 3D segmentation maps of each subject. Following segmentation, we automatically registered the light sheet hemisphere data to the ABA using the MIRACL platform[54,90]. The accuracy of the registration and warping were evaluated using quality control checkpoints. Deformation fields obtained from the registration algorithm were used to warp the ABA labels to the native space of each subject. Finally, we computed the number of cells within each region at depth 6 (labels grouped to a maximum atlas ontology depth of 6, by combining finer labels under their parent labels), by identifying the coordinates of the center of each cell.

To map significant localized group-wise differences in pargyline-yne+ cells in an atlas-agnostic manner, we employed ACE's cluster-wise threshold-free cluster enhancement permutation test using a group-wise ANOVA. The segmentation maps obtained by the deep learning models were downsampled to ABA 10-µm resolution while minimizing information loss by applying a convolution-based voxelization procedure to the whole-brain segmentation maps (based on our prior work[90]). Following voxelization, segmentation maps were aligned with the ABA at a 10-µm resolution using deformation fields obtained via the registration module. The voxelated and warped segmentation maps were then passed to the ACE statistical module (using default parameters), which produced a cluster-wise p-value map representing significant (alpha < 0.05 after correction) localized cell activation between the pargyline-yne treated and control groups.

We computed signal intensity information for each ABA label using the "*miracl lbls stats*" function in our MIRACL platform, which processes NIfTI images and their registered warped

761 ABA labels for each subject. This function extracts key intensity metrics, such as the average,
762 minimum, and maximum voxel intensity, across the input volumes for each label. We further
763 summarized it by grouping labels at depth 6 using the atlas ontology.

764 *Brain-wide drug binding heatmap visualization*

765 Brain regions with positive cell counts in all 5 pargyline-yne-treated hemispheres were included
766 for heatmap generation. Cell density (number of cells per mm^3) was obtained by dividing cell
767 count values by the volume of the brain region. Intensity and cell density were then normalized
768 by the average values in individual hemispheres. Heatmaps were generated using the Python
769 function 'sns.heatmap'[95], with each region displaying the normalized intensity and density across
770 different subjects. The height of each subplot, corresponding to different regions, is proportional
771 to the number of areas within that region. Code for generating heatmaps is available via
772 https://github.com/yelabscripps/vCATCH.

773 **Drug PK analysis**

774 Targeted measurements were performed using an Agilent 6470 triple quadrupole LC-MS
775 instrument. MS analysis was performed using AJS in positive mode. The AJS source parameters
776 were set as follows: the dry gas temperature was set at 250 °C with a gas flow of 12 l/min and the
777 nebulizer pressure at 25 psi; the sheath gas temperature was set to 300 °C with the sheath gas
778 flow set at 12 l/min; and the capillary voltage was set to 3,500 V. Separation of compound was
779 conducted using a ZORBAX RR Eclipse Plus C18 95Å LC column (Agilent 959961-902) with
780 reversed-phase chromatography and the column temperature was maintained at 30 °C. Mobile
781 phases were as follows: buffer A, 100% water with 0.1% formic acid; buffer B, 100%
782 acetonitrile with 0.1% formic acid. The flow rate for each run started at 95% A for 9 minutes at
783 0.7 ml/min, followed by a gradient starting at 95% A, changing linearly to 5% A / 95% B over
784 the course of 12 minutes at 0.7 ml/min. The flow rate was maintained at 5% A / 95% for 6
785 minutes at 0.7 ml/min. The last 3 minutes consisted of a re-equilibration back to 95% A / 5% B at
786 0.7 ml/min. Multiple reaction monitoring was performed for the indicated chemicals with the
787 listed dwell times, fragmentor voltage, collision energies, cell accelerator voltages and polarity.
788 We selected previously reported transitions for the quantification of ibrutinib[96] and afatinib[97].
789 The MS ionization parameters for the targeted metabolomics are presented in Supplemental
790 Table 1. Quantification of the compound concentrations was performed by generating an external
791 standard curve with known concentrations of each compound. Compound standards were
792 analyzed alongside the biological samples using the same targeted triple quadrupole LC/MS
793 method in the same run. A calibration standard curve generated from the compound standard
794 concentrations and total peak areas were used to calculate the concentrations of each compound.
795 It is worth noting that, contrary to the high liver distribution from the autoradiography study[72],
796 our PK data showed overall lesser ibrutinib liver enrichment (Figure S3C). The caveat may be
797 due to the different detection analytes (isotope tag vs. intact free drug). And the observed
798 ibrutinib liver enrichment may reflect strong local metabolism and potential off-target binding.

799

800 **SUPPLEMENTAL INFORMATION**

801 **Supplementary Table 1: Raw data summary and key MS parameters. Related to Figure**
802 **1C, 2D, 2E, 5I, 5J, 5L, 5M, 5O, 5P, S1C, S3B, S3C, S3F, S3G, S5E, S5H.**

803 **Supplementary Video 1: 3D rendering of pargyline-yne binding across the whole mouse**
804 **hemisphere. Related to Figure 1D.**

805 **Supplementary Video 2: 3D rendering of afatinib-yne binding across the whole mouse**
806 **body. Related to Figure S3H, S3J.**

807 **Supplementary Video 3: 3D rendering of ibrutinib-yne binding across the whole mouse**
808 **body. Related to Figure S3H, 3E, S3H.**

809 **REFERENCES**

810 1. Huang, Z., Ogasawara, D., Seneviratne, U.I., Cognetta, A.B., 3rd, Am Ende, C.W.,
811 Nason, D.M., Lapham, K., Litchfield, J., Johnson, D.S., and Cravatt, B.F. (2019). Global
812 Portrait of Protein Targets of Metabolites of the Neurotoxic Compound BIA 10-2474.
813 ACS Chem Biol *14*, 192-197. 10.1021/acschembio.8b01097.

814 2. Chang, J.W., Cognetta, A.B., 3rd, Niphakis, M.J., and Cravatt, B.F. (2013). Proteome-
815 wide reactivity profiling identifies diverse carbamate chemotypes tuned for serine
816 hydrolase inhibition. ACS Chem Biol *8*, 1590-1599. 10.1021/cb400261h.

817 3. Van Esbroeck, A.C., Janssen, A.P., Cognetta, A.B., Ogasawara, D., Shpak, G., Van Der
818 Kroeg, M., Kantae, V., Baggelaar, M.P., De Vrij, F.M., and Deng, H. (2017). Activity-
819 based protein profiling reveals off-target proteins of the FAAH inhibitor BIA 10-2474.
820 Science *356*, 1084-1087. 10.1126/science.aaf7497.

821 4. Reinecke, M., Brear, P., Vornholz, L., Berger, B.T., Seefried, F., Wilhelm, S., Samaras, P.,
822 Gyenis, L., Litchfield, D.W., Medard, G., et al. (2024). Chemical proteomics reveals the
823 target landscape of 1,000 kinase inhibitors. Nat Chem Biol *20*, 577-585. 10.1038/s41589-
824 023-01459-3.

825 5. Offensperger, F., Tin, G., Duran-Frigola, M., Hahn, E., Dobner, S., Ende, C.W.A.,
826 Strohbach, J.W., Rukavina, A., Brennsteiner, V., Ogilvie, K., et al. (2024). Large-scale
827 chemoproteomics expedites ligand discovery and predicts ligand behavior in cells.
828 Science *384*, eadk5864. 10.1126/science.adk5864.

829 6. Shalem, O., Sanjana, N.E., Hartenian, E., Shi, X., Scott, D.A., Mikkelson, T., Heckl, D.,
830 Ebert, B.L., Root, D.E., Doench, J.G., and Zhang, F. (2014). Genome-scale CRISPR-
831 Cas9 knockout screening in human cells. Science *343*, 84-87. 10.1126/science.1247005.

832 7. Zhao, J., Tang, Z., Selvaraju, M., Johnson, K.A., Douglas, J.T., Gao, P.F., Petrassi, H.M.,
833 Wang, M.Z., and Wang, J. (2022). Cellular Target Deconvolution of Small Molecules
834 Using a Selection-Based Genetic Screening Platform. ACS Cent Sci *8*, 1424-1434.
835 10.1021/acscentsci.2c00609.

836 8. Li, H., Ma, T., Remsberg, J.R., Won, S.J., DeMeester, K.E., Njomen, E., Ogasawara, D.,
837 Zhao, K.T., Huang, T.P., Lu, B., et al. (2023). Assigning functionality to cysteines by base
838 editing of cancer dependency genes. Nat Chem Biol *19*, 1320-1330. 10.1038/s41589-023-
839 01428-w.

840 9. Shi, J., Wang, E., Milazzo, J.P., Wang, Z., Kinney, J.B., and Vakoc, C.R. (2015).
841 Discovery of cancer drug targets by CRISPR-Cas9 screening of protein domains. Nat
842 Biotechnol *33*, 661-667. 10.1038/nbt.3235.

843 10. Perrin, J., Werner, T., Kurzawa, N., Rutkowska, A., Childs, D.D., Kalxdorf, M., Poeckel,
844 D., Stonehouse, E., Strohmer, K., Heller, B., et al. (2020). Identifying drug targets in
845 tissues and whole blood with thermal-shift profiling. Nat Biotechnol. 10.1038/s41587-
846 019-0388-4.

847 11. Liu, Z., Wang, P., Wold, E.A., Song, Q., Zhao, C., Wang, C., and Zhou, J. (2021). Small-
848 Molecule Inhibitors Targeting the Canonical WNT Signaling Pathway for the Treatment
849 of Cancer. J Med Chem *64*, 4257-4288. 10.1021/acs.jmedchem.0c01799.

12. Ji, H., Lu, X., Zhao, S., Wang, Q., Liao, B., Bauer, L.G., Huber, K.V.M., Luo, R., Tian, R., and Tan, C.S.H. (2023). Target deconvolution with matrix-augmented pooling strategy reveals cell-specific drug-protein interactions. Cell Chem Biol *30*, 1478-1487 e1477. 10.1016/j.chembiol.2023.08.002.

13. Savitski, M.M., Reinhard, F.B., Franken, H., Werner, T., Savitski, M.F., Eberhard, D., Martinez Molina, D., Jafari, R., Dovega, R.B., Klaeger, S., et al. (2014). Tracking cancer drugs in living cells by thermal profiling of the proteome. Science *346*, 1255784. 10.1126/science.1255784.

14. Stickels, R.R., Murray, E., Kumar, P., Li, J., Marshall, J.L., Di Bella, D.J., Arlotta, P., Macosko, E.Z., and Chen, F. (2020). Highly sensitive spatial transcriptomics at near-cellular resolution with Slide-seqV2. Nature Biotechnology. 10.1038/s41587-020-0739-1.

15. Rodriques, S.G., Stickels, R.R., Goeva, A., Martin, C.A., Murray, E., Vanderburg, C.R., Welch, J., Chen, L.M., Chen, F., and Macosko, E.Z. (2019). Slide-seq: A scalable technology for measuring genome-wide expression at high spatial resolution. Science *363*, 1463-1467. 10.1126/science.aaw1219.

16. Bhatia, H.S., Brunner, A.-D., Öztürk, F., Kapoor, S., Rong, Z., Mai, H., Thielert, M., Ali, M., Al-Maskari, R., Paetzold, J.C., et al. (2022). Spatial proteomics in three-dimensional intact specimens. Cell *185*, 5040-5058.e5019. 10.1016/j.cell.2022.11.021.

17. Unterauer, E.M., Shetab Boushehri, S., Jevdokimenko, K., Masullo, L.A., Ganji, M., Sograte-Idrissi, S., Kowalewski, R., Strauss, S., Reinhardt, S.C.M., Perovic, A., et al. (2024). Spatial proteomics in neurons at single-protein resolution. Cell *187*, 1785-1800.e1716. 10.1016/j.cell.2024.02.045.

18. Hickey, J.W., Neumann, E.K., Radtke, A.J., Camarillo, J.M., Beuschel, R.T., Albanese, A., McDonough, E., Hatler, J., Wiblin, A.E., Fisher, J., et al. (2021). Spatial mapping of protein composition and tissue organization: a primer for multiplexed antibody-based imaging. Nat Methods. 10.1038/s41592-021-01316-y.

19. Shi, H., He, Y., Zhou, Y., Huang, J., Maher, K., Wang, B., Tang, Z., Luo, S., Tan, P., Wu, M., et al. (2023). Spatial atlas of the mouse central nervous system at molecular resolution. Nature. 10.1038/s41586-023-06569-5.

20. Zeng, H., Huang, J., Ren, J., Wang, C.K., Tang, Z., Zhou, H., Zhou, Y., Shi, H., Aditham, A., Sui, X., et al. (2023). Spatially resolved single-cell translatomics at molecular resolution. Science *380*, eadd3067. 10.1126/science.add3067.

21. Pang, Z., Schafroth, M.A., Ogasawara, D., Wang, Y., Nudell, V., Lal, N.K., Yang, D., Wang, K., Herbst, D.M., Ha, J., et al. (2022). In situ identification of cellular drug targets in mammalian tissue. Cell *185*, 1793-1805 e1717. 10.1016/j.cell.2022.03.040.

22. Sylwestrak, E.L., Rajasethupathy, P., Wright, M.A., Jaffe, A., and Deisseroth, K. (2016). Multiplexed Intact-Tissue Transcriptional Analysis at Cellular Resolution. Cell *164*, 792-804. 10.1016/j.cell.2016.01.038.

23. Murray, E., Cho, J.H., Goodwin, D., Ku, T., Swaney, J., Kim, S.Y., Choi, H., Park, Y.G., Park, J.Y., Hubbert, A., et al. (2015). Simple, Scalable Proteomic Imaging for High-Dimensional Profiling of Intact Systems. Cell *163*, 1500-1514. 10.1016/j.cell.2015.11.025.

892 24. Mai, H., Luo, J., Hoeher, L., Al-Maskari, R., Horvath, I., Chen, Y., Kofler, F., Piraud, M.,
893 Paetzold, J.C., Modamio, J., et al. (2023). Whole-body cellular mapping in mouse using
894 standard IgG antibodies. Nat Biotechnol. 10.1038/s41587-023-01846-0.

895 25. Wang, X., Allen, W.E., Wright, M.A., Sylwestrak, E.L., Samusik, N., Vesuna, S., Evans,
896 K., Liu, C., Ramakrishnan, C., Liu, J., et al. (2018). Three-dimensional intact-tissue
897 sequencing of single-cell transcriptional states. Science *361*. 10.1126/science.aat5691.

898 26. Tyler, D.S., Vappiani, J., Cañeque, T., Lam, E.Y., Ward, A., Gilan, O., Chan, Y.-C.,
899 Hienzsch, A., Rutkowska, A., and Werner, T. (2017). Click chemistry enables preclinical
900 evaluation of targeted epigenetic therapies. Science *356*, 1397-1401.

901 27. Nudell, V., Wang, Y., Pang, Z., Lal, N.K., Huang, M., Shaabani, N., Kanim, W., Teijaro,
902 J., Maximov, A., and Ye, L. (2022). HYBRiD: hydrogel-reinforced DISCO for clearing
903 mammalian bodies. Nat Methods. 10.1038/s41592-022-01427-0.

904 28. Murakami, T.C., Mano, T., Saikawa, S., Horiguchi, S.A., Shigeta, D., Baba, K., Sekiya,
905 H., Shimizu, Y., Tanaka, K.F., Kiyonari, H., et al. (2018). A three-dimensional single-cell-
906 resolution whole-brain atlas using CUBIC-X expansion microscopy and tissue clearing.
907 Nat Neurosci *21*, 625-637. 10.1038/s41593-018-0109-1.

908 29. Kim, S.Y., Cho, J.H., Murray, E., Bakh, N., Choi, H., Ohn, K., Ruelas, L., Hubbert, A.,
909 McCue, M., Vassallo, S.L., et al. (2015). Stochastic electrotransport selectively enhances
910 the transport of highly electromobile molecules. Proc Natl Acad Sci U S A *112*, E6274-
911 6283. 10.1073/pnas.1510133112.

912 30. Tainaka, K., Murakami, T.C., Susaki, E.A., Shimizu, C., Saito, R., Takahashi, K.,
913 Hayashi-Takagi, A., Sekiya, H., Arima, Y., Nojima, S., et al. (2018). Chemical Landscape
914 for Tissue Clearing Based on Hydrophilic Reagents. Cell Rep *24*, 2196-2210 e2199.
915 10.1016/j.celrep.2018.07.056.

916 31. Park, J., Wang, J., Guan, W., Gjesteby, L.A., Pollack, D., Kamentsky, L., Evans, N.B.,
917 Stirman, J., Gu, X., Zhao, C., et al. (2024). Integrated platform for multiscale molecular
918 imaging and phenotyping of the human brain. Science *384*, eadh9979.
919 10.1126/science.adh9979.

920 32. Ku, T., Guan, W., Evans, N.B., Sohn, C.H., Albanese, A., Kim, J.-G., Frosch, M.P., and
921 Chung, K. (2020). Elasticizing tissues for reversible shape transformation and accelerated
922 molecular labeling. Nat Methods *17*, 609-613.

923 33. Lai, H.M., Tang, Y., Lau, Z.Y.H., Campbell, R.A.A., Yau, J.C.N., Chan, C.C.Y., Chan,
924 D.C.W., Wong, T.Y., Wong, H.K.T., Yan, L.Y.C., et al. (2022). Antibody stabilization for
925 thermally accelerated deep immunostaining. Nat Methods *19*, 1137-1146.
926 10.1038/s41592-022-01569-1.

927 34. Susaki, E.A., Shimizu, C., Kuno, A., Tainaka, K., Li, X., Nishi, K., Morishima, K., Ono,
928 H., Ode, K.L., Saeki, Y., et al. (2020). Versatile whole-organ/body staining and imaging
929 based on electrolyte-gel properties of biological tissues. Nat Commun *11*, 1982.
930 10.1038/s41467-020-15906-5.

931 35. Zhao, S., Todorov, M.I., Cai, R., Maskari, R.A.I., Steinke, H., Kemter, E., Mai, H., Rong,
932 Z., Warmer, M., Stanic, K., et al. (2020). Cellular and Molecular Probing of Intact Human
933 Organs. Cell. 10.1016/j.cell.2020.01.030.

934 36. Choi, S.W., Guan, W., and Chung, K. (2021). Basic principles of hydrogel-based tissue
935 transformation technologies and their applications. Cell *184*, 4115-4136.
936 10.1016/j.cell.2021.07.009.

937 37. Yau, C.N., Lai, H.M., Lee, K., Kwok, A.J., Huang, J., and Ko, H. (2023). Principles of
938 deep immunohistochemistry for 3D histology. Cell Rep Methods *3*, 100458.
939 10.1016/j.crmeth.2023.100458.

940 38. Richardson, D.S., Guan, W., Matsumoto, K., Pan, C., Chung, K., Erturk, A., Ueda, H.R.,
941 and Lichtman, J.W. (2021). Tissue Clearing. Nat Rev Methods Primers *1*.
942 10.1038/s43586-021-00080-9.

943 39. Ueda, H.R., Erturk, A., Chung, K., Gradinaru, V., Chedotal, A., Tomancak, P., and Keller,
944 P.J. (2020). Tissue clearing and its applications in neuroscience. Nat Rev Neurosci *21*, 61-
945 79. 10.1038/s41583-019-0250-1.

946 40. Dejaegere, A., Choulier, L., Lafont, V., De Genst, E., and Altschuh, D. (2005). Variations
947 in Antigen− Antibody Association Kinetics as a Function of pH and Salt Concentration: A
948 QSAR and Molecular Modeling Study. Biochemistry *44*, 14409-14418.

949 41. Cann, J.R., and Clark, E.W. (1956). Kinetics of the Antigen-Antibody Reaction. Effect of
950 Salt Concentration and pH on the Rate of Neutralization of Bacteriophage by Purified
951 Fractions of Specific Antiserum1a, b. J Am Chem Soc *78*, 3627-3631.

952 42. Himo, F., Lovell, T., Hilgraf, R., Rostovtsev, V.V., Noodleman, L., Sharpless, K.B., and
953 Fokin, V.V. (2005). Copper (I)-catalyzed synthesis of azoles. DFT study predicts
954 unprecedented reactivity and intermediates. J Am Chem Soc *127*, 210-216.

955 43. Krysiak, J.M., Kreuzer, J., Macheroux, P., Hermetter, A., Sieber, S.A., and Breinbauer, R.
956 (2012). Activity-based probes for studying the activity of flavin-dependent oxidases and
957 for the protein target profiling of monoamine oxidase inhibitors. Angew Chem Int Ed
958 Engl *51*, 7035-7040. 10.1002/anie.201201955.

959 44. Niphakis, M.J., Johnson, D.S., Ballard, T.E., Stiff, C., and Cravatt, B.F. (2012). O-
960 hydroxyacetamide carbamates as a highly potent and selective class of endocannabinoid
961 hydrolase inhibitors. ACS Chem Neurosci *3*, 418-426. 10.1021/cn200089j.

962 45. Festa, R.A., and Thiele, D.J. (2011). Copper: an essential metal in biology. Curr Biol *21*,
963 R877-883. 10.1016/j.cub.2011.09.040.

964 46. Inesi, G. (2017). Molecular features of copper binding proteins involved in copper
965 homeostasis. IUBMB Life *69*, 211-217. 10.1002/iub.1590.

966 47. Andreini, C., Banci, L., Bertini, I., and Rosato, A. (2008). Occurrence of copper proteins
967 through the three domains of life: a bioinformatic approach. The Journal of Proteome
968 Research *7*, 209-216.

969 48. Selden, C.R., Schilling, K., Godfrey, L., and Yee, N. (2024). Metal-binding amino acid
970 ligands commonly found in metalloproteins differentially fractionate copper isotopes. Sci
971 Rep *14*, 1902. 10.1038/s41598-024-52091-7.

972 49. Li, S., Cai, H., He, J., Chen, H., Lam, S., Cai, T., Zhu, Z., Bark, S.J., and Cai, C. (2016).
973 Extent of the Oxidative Side Reactions to Peptides and Proteins During the CuAAC
974 Reaction. Bioconjug Chem *27*, 2315-2322. 10.1021/acs.bioconjchem.6b00267.

975 50. Abel, G.R., Jr., Calabrese, Z.A., Ayco, J., Hein, J.E., and Ye, T. (2016). Measuring and
976 Suppressing the Oxidative Damage to DNA During Cu(I)-Catalyzed Azide-Alkyne
977 Cycloaddition. Bioconjug Chem *27*, 698-704. 10.1021/acs.bioconjchem.5b00665.

978 51. Wiest, A., and Kielkowski, P. (2024). Cu-Catalyzed Azide-Alkyne-Thiol Reaction Forms
979 Ubiquitous Background in Chemical Proteomic Studies. J Am Chem Soc.
980 10.1021/jacs.3c11780.

981 52. Attarpour, A., Osmann, J., Rinaldi, A., Qi, T., Lal, N., Patel, S., Rozak, M., Yu, F., Cho,
982 N., Squair, J., et al. (2025). A deep learning pipeline for three-dimensional brain-wide
983 mapping of local neuronal ensembles in teravoxel light-sheet microscopy. Nat Methods
984 *22*, 600-611. 10.1038/s41592-024-02583-1.

985 53. Attarpour, A., Osmann, J., Rinaldi, A., Qi, T., Lal, N., Patel, S., Rozak, M., Yu, F., Cho,
986 N., Squair, J., et al. A deep learning pipeline for 3D brain-wide mapping of local neuronal
987 ensembles in tera-voxel light sheet microscopy. Nat Methods *in press*.

988 54. Wang, Q., Ding, S.-L., Li, Y., Royall, J., Feng, D., Lesnar, P., Graddis, N., Naeemi, M.,
989 Facer, B., and Ho, A. (2020). The Allen mouse brain common coordinate framework: a
990 3D reference atlas. Cell *181*, 936-953. e920.

991 55. Boike, L., Henning, N.J., and Nomura, D.K. (2022). Advances in covalent drug
992 discovery. Nat Rev Drug Discov. 10.1038/s41573-022-00542-z.

993 56. Ghosh, A.K., Samanta, I., Mondal, A., and Liu, W.R. (2019). Covalent Inhibition in Drug
994 Discovery. ChemMedChem *14*, 889-906. 10.1002/cmdc.201900107.

995 57. Miller, V.A., Hirsh, V., Cadranel, J., Chen, Y.-M., Park, K., Kim, S.-W., Zhou, C., Su, W.-
996 C., Wang, M., Sun, Y., et al. (2012). Afatinib versus placebo for patients with advanced,
997 metastatic non-small-cell lung cancer after failure of erlotinib, gefitinib, or both, and one
998 or two lines of chemotherapy (LUX-Lung 1): a phase 2b/3 randomised trial. The Lancet
999 Oncology *13*, 528-538. 10.1016/s1470-2045(12)70087-6.

1000 58. Sequist, L.V., Yang, J.C., Yamamoto, N., O'Byrne, K., Hirsh, V., Mok, T., Geater, S.L.,
1001 Orlov, S., Tsai, C.M., Boyer, M., et al. (2013). Phase III study of afatinib or cisplatin plus
1002 pemetrexed in patients with metastatic lung adenocarcinoma with EGFR mutations. J
1003 Clin Oncol *31*, 3327-3334. 10.1200/jco.2012.44.2806.

1004 59. Byrd, J.C., Furman, R.R., Coutre, S.E., Flinn, I.W., Burger, J.A., Blum, K.A., Grant, B.,
1005 Sharman, J.P., Coleman, M., Wierda, W.G., et al. (2013). Targeting BTK with ibrutinib in
1006 relapsed chronic lymphocytic leukemia. N Engl J Med *369*, 32-42.
1007 10.1056/NEJMoa1215637.

1008 60. Treon, S.P., Tripsas, C.K., Meid, K., Warren, D., Varma, G., Green, R., Argyropoulos,
1009 K.V., Yang, G., Cao, Y., Xu, L., et al. (2015). Ibrutinib in previously treated
1010 Waldenstrom's macroglobulinemia. N Engl J Med *372*, 1430-1440.
1011 10.1056/NEJMoa1501548.

1012 61. Wang, M.L., Rule, S., Martin, P., Goy, A., Auer, R., Kahl, B.S., Jurczak, W., Advani,
1013 R.H., Romaguera, J.E., Williams, M.E., et al. (2013). Targeting BTK with ibrutinib in
1014 relapsed or refractory mantle-cell lymphoma. N Engl J Med *369*, 507-516.
1015 10.1056/NEJMoa1306220.

1016 62. Yun, S., Vincelette, N.D., Acharya, U., and Abraham, I. (2017). Risk of Atrial Fibrillation
1017 and Bleeding Diathesis Associated With Ibrutinib Treatment: A Systematic Review and
1018 Pooled Analysis of Four Randomized Controlled Trials. Clin Lymphoma Myeloma Leuk
1019 *17*, 31-37 e13. 10.1016/j.clml.2016.09.010.

1020 63. Lipsky, A.H., Farooqui, M.Z., Tian, X., Martyr, S., Cullinane, A.M., Nghiem, K., Sun, C.,
1021 Valdez, J., Niemann, C.U., Herman, S.E., et al. (2015). Incidence and risk factors of
1022 bleeding-related adverse events in patients with chronic lymphocytic leukemia treated
1023 with ibrutinib. Haematologica *100*, 1571-1578. 10.3324/haematol.2015.126672.

1024 64. Berglof, A., Hamasy, A., Meinke, S., Palma, M., Krstic, A., Mansson, R., Kimby, E.,
1025 Osterborg, A., and Smith, C.I. (2015). Targets for Ibrutinib Beyond B Cell Malignancies.
1026 Scand J Immunol *82*, 208-217. 10.1111/sji.12333.

1027 65. Tuomi, J.M., Xenocostas, A., and Jones, D.L. (2018). Increased Susceptibility for Atrial
1028 and Ventricular Cardiac Arrhythmias in Mice Treated With a Single High Dose of
1029 Ibrutinib. Can J Cardiol *34*, 337-341. 10.1016/j.cjca.2017.12.001.

1030 66. Xiao, L., Salem, J.E., Clauss, S., Hanley, A., Bapat, A., Hulsmans, M., Iwamoto, Y.,
1031 Wojtkiewicz, G., Cetinbas, M., Schloss, M.J., et al. (2020). Ibrutinib-Mediated Atrial
1032 Fibrillation Attributable to Inhibition of C-Terminal Src Kinase. Circulation *142*, 2443-
1033 2455. 10.1161/CIRCULATIONAHA.120.049210.

1034 67. McMullen, J.R., Boey, E.J., Ooi, J.Y., Seymour, J.F., Keating, M.J., and Tam, C.S.
1035 (2014). Ibrutinib increases the risk of atrial fibrillation, potentially through inhibition of
1036 cardiac PI3K-Akt signaling. Blood, The Journal of the American Society of Hematology
1037 *124*, 3829-3830.

1038 68. Honigberg, L.A., Smith, A.M., Sirisawad, M., Verner, E., Loury, D., Chang, B., Li, S.,
1039 Pan, Z., Thamm, D.H., Miller, R.A., and Buggy, J.J. (2010). The Bruton tyrosine kinase
1040 inhibitor PCI-32765 blocks B-cell activation and is efficacious in models of autoimmune
1041 disease and B-cell malignancy. Proc Natl Acad Sci U S A *107*, 13075-13080.
1042 10.1073/pnas.1004594107.

1043 69. Lanning, B.R., Whitby, L.R., Dix, M.M., Douhan, J., Gilbert, A.M., Hett, E.C., Johnson,
1044 T.O., Joslyn, C., Kath, J.C., Niessen, S., et al. (2014). A road map to evaluate the
1045 proteome-wide selectivity of covalent kinase inhibitors. Nat Chem Biol *10*, 760-767.
1046 10.1038/nchembio.1582.

1047 70. Kaltenecker, D., Al-Maskari, R., Negwer, M., Hoeher, L., Kofler, F., Zhao, S., Todorov,
1048 M., Rong, Z., Paetzold, J.C., Wiestler, B., et al. (2024). Virtual reality-empowered deep-
1049 learning analysis of brain cells. Nat Methods *21*, 1306-1315. 10.1038/s41592-024-02245-
1050 2.

1051 71. CENTER FOR DRUG EVALUATION AND RESEARCH APPLICATION NUMBER:
1052 201292Orig1s000. (2013).
1053 https://www.accessdata.fda.gov/drugsatfda_docs/nda/2013/201292Orig1s000PharmR.pdf
1054 .

1055 72. CENTER FOR DRUG EVALUATION AND RESEARCH APPLICATION NUMBER:
1056 205552Orig2s000. (2014).

https://www.accessdata.fda.gov/drugsatfda_docs/nda/2013/205552Orig1s000PharmR.pdf .

73. Karlsson, M., Zhang, C., Méar, L., Zhong, W., Digre, A., Katona, B., Sjöstedt, E., Butler, L., Odeberg, J., Dusart, P., et al. (2021). A single–cell type transcriptomics map of human tissues. Science Advances *7*, eabh2169. doi:10.1126/sciadv.abh2169.

74. Xie, J., Zhang, J., Wu, H., Tang, X., Liu, J., Cheng, G., and Li, P. (2017). The influences of age on T lymphocyte subsets in C57BL/6 mice. Saudi J Biol Sci *24*, 108-113. 10.1016/j.sjbs.2016.09.002.

75. Fleming, M.R., Xiao, L., Jackson, K.D., Beckman, J.A., Barac, A., and Moslehi, J.J. (2021). Vascular Impact of Cancer Therapies: The Case of BTK (Bruton Tyrosine Kinase) Inhibitors. Circ Res *128*, 1973-1987. 10.1161/CIRCRESAHA.121.318259.

76. Ryan, C.E., Sahaf, B., Logan, A.C., O'Brien, S., Byrd, J.C., Hillmen, P., Brown, J.R., Dyer, M.J., Mato, A.R., Keating, M.J., et al. (2016). Ibrutinib efficacy and tolerability in patients with relapsed chronic lymphocytic leukemia following allogeneic HCT. Blood *128*, 2899-2908. 10.1182/blood-2016-06-715284.

77. Tom Dieck, S., Muller, A., Nehring, A., Hinz, F.I., Bartnik, I., Schuman, E.M., and Dieterich, D.C. (2012). Metabolic labeling with noncanonical amino acids and visualization by chemoselective fluorescent tagging. Curr Protoc Cell Biol *Chapter 7*, 7 11 11-17 11 29. 10.1002/0471143030.cb0711s56.

78. Jao, C.Y., and Salic, A. (2008). Exploring RNA transcription and turnover in vivo by using click chemistry. Proc Natl Acad Sci U S A *105*, 15779-15784.

79. Nikic, I., Kang, J.H., Girona, G.E., Aramburu, I.V., and Lemke, E.A. (2015). Labeling proteins on live mammalian cells using click chemistry. Nat Protoc *10*, 780-791. 10.1038/nprot.2015.045.

80. El-Sagheer, A.H., and Brown, T. (2010). Click chemistry with DNA. Chemical Society Reviews *39*, 1388-1405.

81. Soriano del Amo, D., Wang, W., Jiang, H., Besanceney, C., Yan, A.C., Levy, M., Liu, Y., Marlow, F.L., and Wu, P. (2010). Biocompatible copper (I) catalysts for in vivo imaging of glycans. J Am Chem Soc *132*, 16893-16899.

82. Hulce, J.J., Cognetta, A.B., Niphakis, M.J., Tully, S.E., and Cravatt, B.F. (2013). Proteome-wide mapping of cholesterol-interacting proteins in mammalian cells. Nat Methods *10*, 259-264. 10.1038/nmeth.2368.

83. Tamura, I., Sakamoto, D.M., Yi, B., Saito, Y., Yamada, N., Morimoto, J., Takakusagi, Y., Kuroda, M., Kubota, S.I., and Yatabe, H. (2024). Click3D: Click reaction across deep tissues for whole-organ 3D fluorescence imaging. Science Advances *10*, eado8471.

84. Shi, M.Y., Yao, Y., Wang, M., Yang, Q., Ding, L., Li, R., Li, Y., Huang, H., Yang, C.Y., Zhou, Z., et al. (2025). High-speed mapping of whole-mouse peripheral nerves at subcellular resolution. Cell *188*, 3897-3915 e3820. 10.1016/j.cell.2025.06.011.

85. Xu, F., Shen, Y., Ding, L., Yang, C.Y., Tan, H., Wang, H., Zhu, Q., Xu, R., Wu, F., Xiao, Y., et al. (2021). High-throughput mapping of a whole rhesus monkey brain at micrometer resolution. Nat Biotechnol *39*, 1521-1528. 10.1038/s41587-021-00986-5.

86. Verstegen, A.M.J., Vanderhorst, V., Gray, P.A., Zeidel, M.L., and Geerling, J.C. (2017). Barrington's nucleus: Neuroanatomic landscape of the mouse "pontine micturition center". J Comp Neurol *525*, 2287-2309. 10.1002/cne.24215.

87. Chung, K., Wallace, J., Kim, S.Y., Kalyanasundaram, S., Andalman, A.S., Davidson, T.J., Mirzabekov, J.J., Zalocusky, K.A., Mattis, J., Denisin, A.K., et al. (2013). Structural and molecular interrogation of intact biological systems. Nature *497*, 332-337. 10.1038/nature12107.

88. Qi, Y., Yu, T., Xu, J., Wan, P., Ma, Y., Zhu, J., Li, Y., Gong, H., Luo, Q., and Zhu, D. (2019). FDISCO: Advanced solvent-based clearing method for imaging whole organs. Science Advances *5*, eaau8355. 10.1126/sciadv.aau8355.

89. Park, Y.G., Sohn, C.H., Chen, R., McCue, M., Yun, D.H., Drummond, G.T., Ku, T., Evans, N.B., Oak, H.C., Trieu, W., et al. (2018). Protection of tissue physicochemical properties using polyfunctional crosslinkers. Nat Biotechnol *37*, 73-83. 10.1038/nbt.4281.

90. Goubran, M., Leuze, C., Hsueh, B., Aswendt, M., Ye, L., Tian, Q., Cheng, M.Y., Crow, A., Steinberg, G.K., and McNab, J.A. (2019). Multimodal image registration and connectivity analysis for integration of connectomic data from microscopy to MRI. Nature communications *10*, 5504.

91. Arzt, M., Deschamps, J., Schmied, C., Pietzsch, T., Schmidt, D., Tomancak, P., Haase, R., and Jug, F. (2022). LABKIT: labeling and segmentation toolkit for big image data. Frontiers in computer science *4*, 777728.

92. Schindelin, J., Arganda-Carreras, I., Frise, E., Kaynig, V., Longair, M., Pietzsch, T., Preibisch, S., Rueden, C., Saalfeld, S., Schmid, B., et al. (2012). Fiji: an open-source platform for biological-image analysis. Nat Methods *9*, 676-682. 10.1038/nmeth.2019.

93. Kinga, D., and Adam, J.B. (2015). A method for stochastic optimization. (San Diego, California;), pp. 6.

94. Wagner, T., and Lipinski, H.-G. (2013). IJBlob: an ImageJ library for connected component analysis and shape analysis. Journal of Open Research Software *1*.

95. Waskom, M.L. (2021). Seaborn: statistical data visualization. Journal of Open Source Software *6*, 3021.

96. Tang, P.-f., Bao, S.-s., Xiao, Z.-x., Xie, W.-f., Wu, X.-m., Ge, H.-l., and Shao, C.-f. (2023). A novel UHPLC–MS/MS method for quantitative analysis of zanubrutinib in rat plasma: application to an in vivo interaction study between zanubrutinib and triazole antifungal. BMC chemistry *17*, 107.

97. Lu, X., Liu, S., Yang, X., Han, M., and Sun, K. (2019). Determination of tyrosine kinase inhibitor afatinib in rat plasma using LC–MS/MS and its application to in vivo pharmacokinetic studies of afatinib liposomes. Journal of Pharmaceutical and Biomedical Analysis *164*, 181-186.

Figure 1

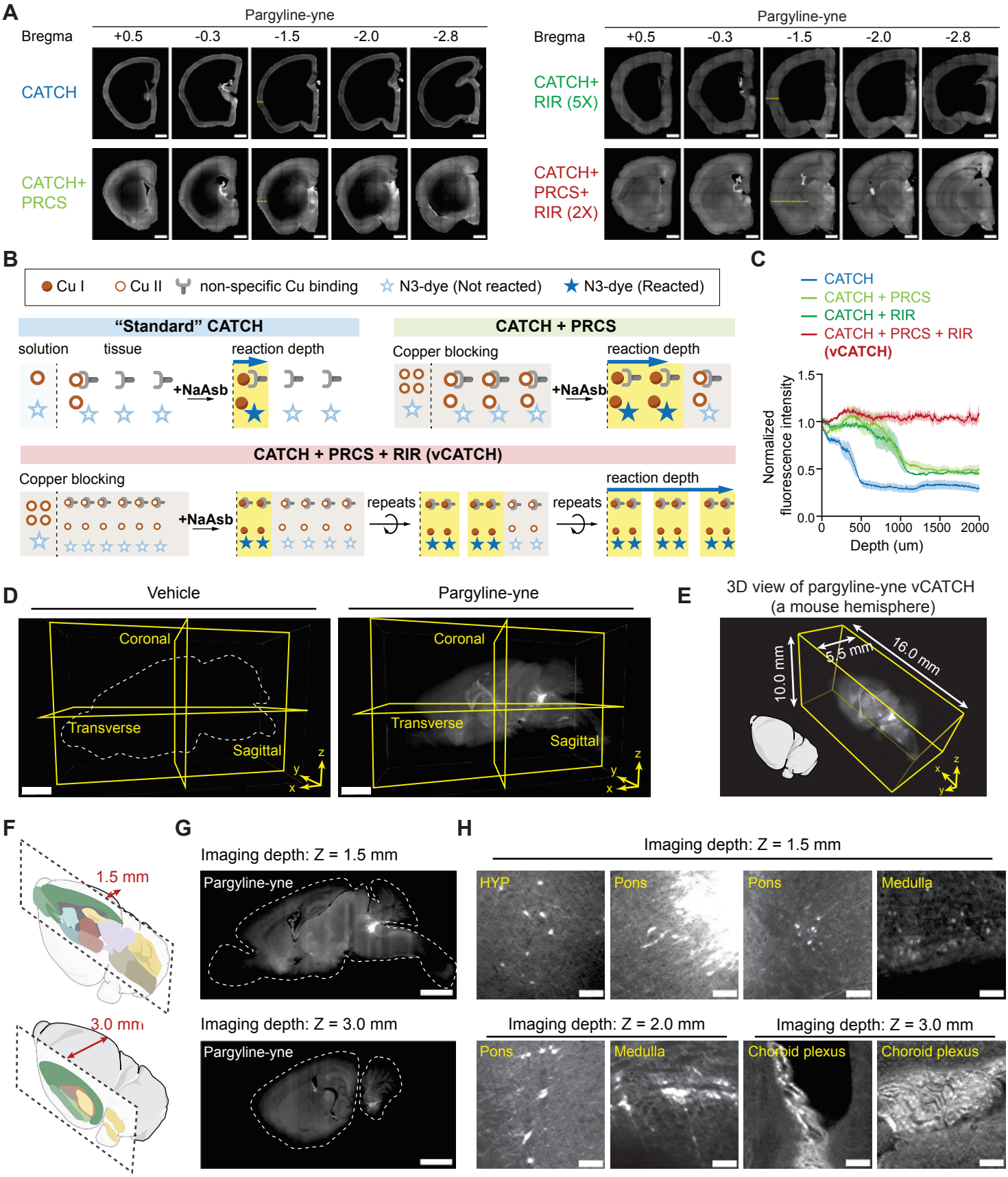
A
Pargyline-yne
Bregma
+0.5
-0.3
-1.5
-2.0
-2.8
CATCH
CATCH+ PRCS
CATCH+ RIR (5X)
CATCH+ PRCS+ RIR (2X)
B
Cu I
Cu II
non-specific Cu binding
N3-dye (Not reacted)
N3-dye (Reacted)
"Standard" CATCH
solution
tissue
reaction depth
+NaAsb
CATCH + PRCS
Copper blocking
CATCH + PRCS + RIR (vCATCH)
repeats
C
CATCH
CATCH + PRCS
CATCH + RIR
CATCH + PRCS + RIR (vCATCH)
Normalized fluorescence intensity
Depth (um)
D
Vehicle
Pargyline-yne
Coronal
Transverse
Sagittal
E
3D view of pargyline-yne vCATCH (a mouse hemisphere)
10.0 mm
5.5 mm
16.0 mm
F
1.5 mm
3.0 mm
G
Imaging depth: Z = 1.5 mm
Pargyline-yne
Imaging depth: Z = 3.0 mm
H
Imaging depth: Z = 1.5 mm
HYP
Pons
Medulla
Imaging depth: Z = 2.0 mm
Imaging depth: Z = 3.0 mm
Choroid plexus

Figure 2

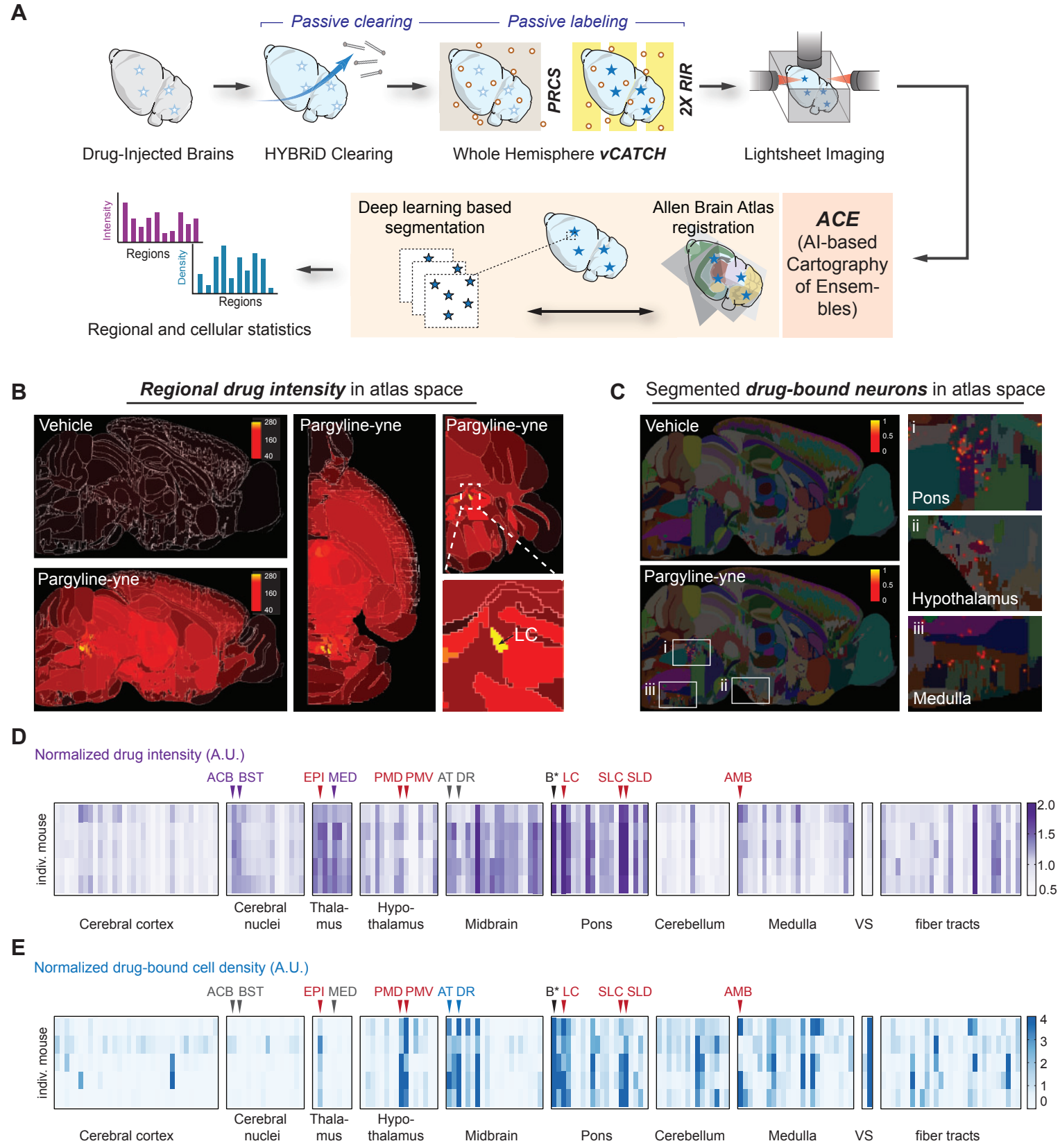
A
Passive clearing
Passive labeling
PRCS
2X RIR
Drug-Injected Brains
HYBRiD Clearing
Whole Hemisphere vCATCH
Lightsheet Imaging
Intensity
Regions
Density
Regions
Regional and cellular statistics
Deep learning based segmentation
Allen Brain Atlas registration
ACE (AI-based Cartography of Ensem-bles)
B
Regional drug intensity in atlas space
Vehicle
Pargyline-yne
Pargyline-yne
Pargyline-yne
LC
C
Segmented drug-bound neurons in atlas space
Vehicle
Pargyline-yne
i
ii
iii
Pons
Hypothalamus
Medulla
D
Normalized drug intensity (A.U.)
ACB BST
EPI MED
PMD PMV
AT DR
B* LC
SLC SLD
AMB
indiv. mouse
Cerebral cortex
Cerebral nuclei
Thala-mus
Hypo-thalamus
Midbrain
Pons
Cerebellum
Medulla
VS
fiber tracts
E
Normalized drug-bound cell density (A.U.)
ACB BST
EPI MED
PMD PMV
AT DR
B* LC
SLC SLD
AMB
indiv. mouse
Cerebral cortex
Cerebral nuclei
Thala-mus
Hypo-thalamus
Midbrain
Pons
Cerebellum
Medulla
VS
fiber tracts

Figure 3

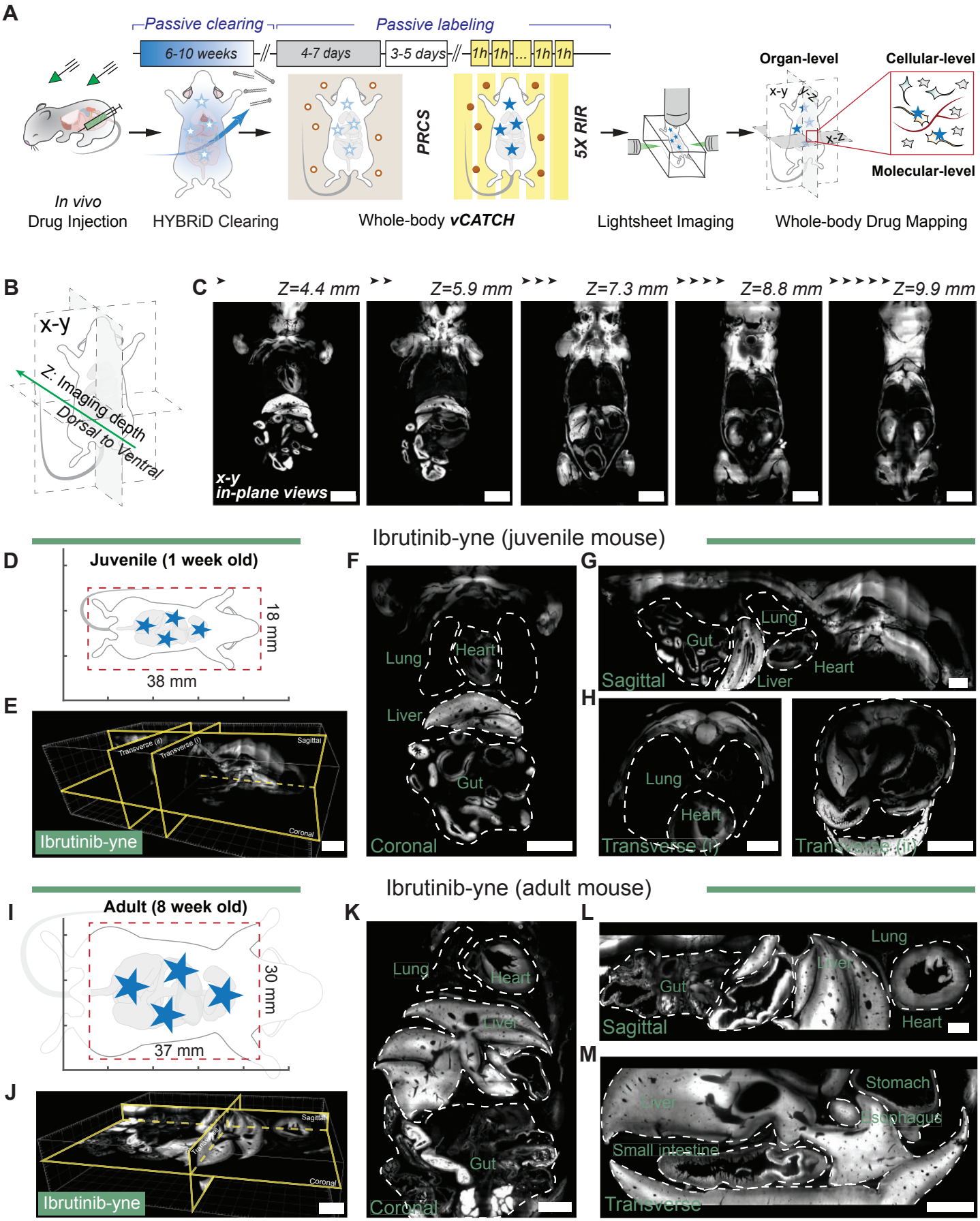
A
Passive clearing
Passive labeling
6-10 weeks
4-7 days
3-5 days
1h
1h
...
1h
1h
PRCS
5X RIR
Organ-level
Cellular-level
Molecular-level
x-y
x-z
y-z
In vivo
Drug Injection
HYBRiD Clearing
Whole-body vCATCH
Lightsheet Imaging
Whole-body Drug Mapping
B
x-y
Z: Imaging depth
Dorsal to Ventral
C
Z=4.4 mm
Z=5.9 mm
Z=7.3 mm
Z=8.8 mm
Z=9.9 mm
x-y
in-plane views
Ibrutinib-yne (juvenile mouse)
D
Juvenile (1 week old)
18 mm
38 mm
E
Transverse (II)
Transverse (I)
Sagittal
Coronal
Ibrutinib-yne
F
Lung
Heart
Liver
Gut
Coronal
G
Lung
Gut
Heart
Liver
Sagittal
H
Lung
Heart
Transverse (I)
Transverse (II)
Ibrutinib-yne (adult mouse)
I
Adult (8 week old)
30 mm
37 mm
J
Sagittal
Transverse
Coronal
Ibrutinib-yne
K
Lung
Heart
Liver
Gut
Coronal
L
Lung
Liver
Gut
Heart
Sagittal
M
Stomach
Liver
Esophagus
Small intestine
Transverse

Figure 4

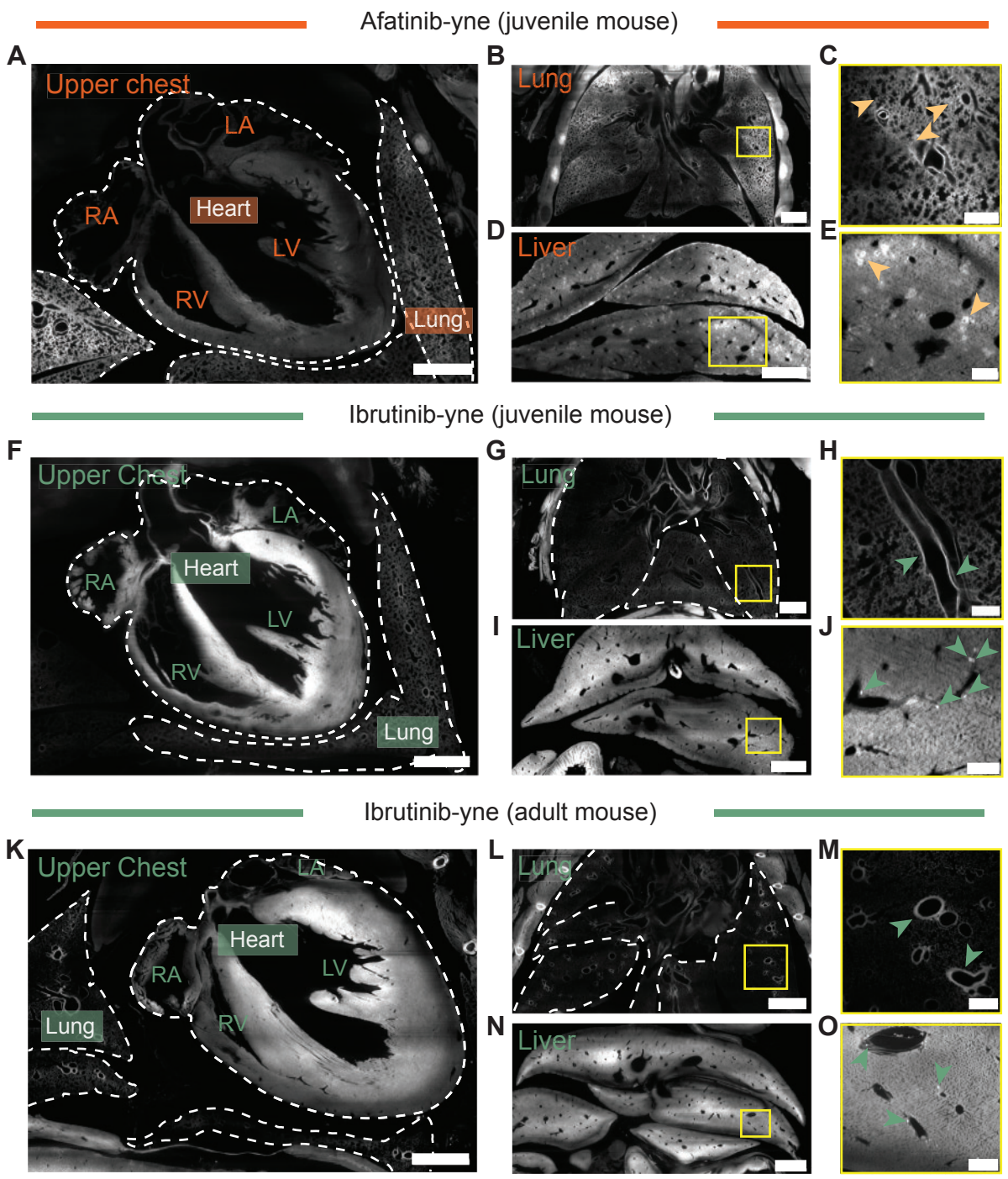
Afatinib-yne (juvenile mouse)
A
Upper chest
LA
RA
Heart
LV
RV
Lung
B
Lung
C
D
Liver
E
Ibrutinib-yne (juvenile mouse)
F
Upper Chest
LA
RA
Heart
LV
RV
Lung
G
Lung
H
I
Liver
J
Ibrutinib-yne (adult mouse)
K
Upper Chest
LA
Heart
RA
LV
Lung
RV
L
Lung
M
N
Liver
O

Figure 5

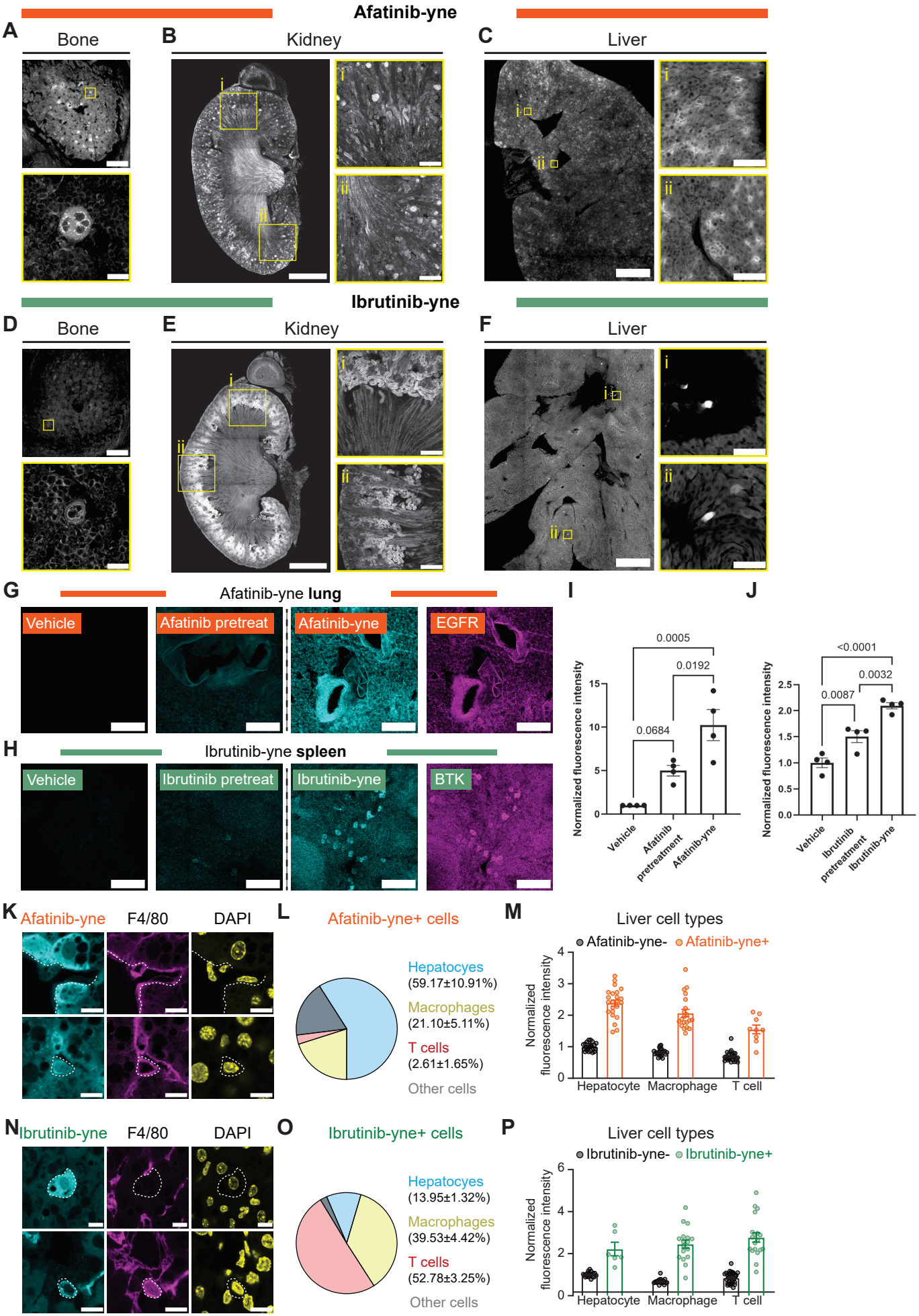
Afatinib-yne
A
Bone
B
Kidney
C
Liver
Ibrutinib-yne
D
Bone
E
Kidney
F
Liver
G
Afatinib-yne lung
Vehicle
Afatinib pretreat
Afatinib-yne
EGFR
H
Ibrutinib-yne spleen
Vehicle
Ibrutinib pretreat
Ibrutinib-yne
BTK
I
Normalized fluorescence intensity
0.0005
0.0192
0.0684
Vehicle
Afatinib pretreatment
Afatinib-yne
J
Normalized fluorescence intensity
<0.0001
0.0032
0.0087
Vehicle
Ibrutinib pretreatment
Ibrutinib-yne
K
Afatinib-yne
F4/80
DAPI
L
Afatinib-yne+ cells
Hepatocyes (59.17±10.91%)
Macrophages (21.10±5.11%)
T cells (2.61±1.65%)
Other cells
M
Liver cell types
Afatinib-yne-
Afatinib-yne+
Normalized fluorescence intensity
Hepatocyte
Macrophage
T cell
N
Ibrutinib-yne
F4/80
DAPI
O
Ibrutinib-yne+ cells
Hepatocyes (13.95±1.32%)
Macrophages (39.53±4.42%)
T cells (52.78±3.25%)
Other cells
P
Liver cell types
Ibrutinib-yne-
Ibrutinib-yne+
Normalized fluorescence intensity
Hepatocyte
Macrophage
T cell

Figure S1

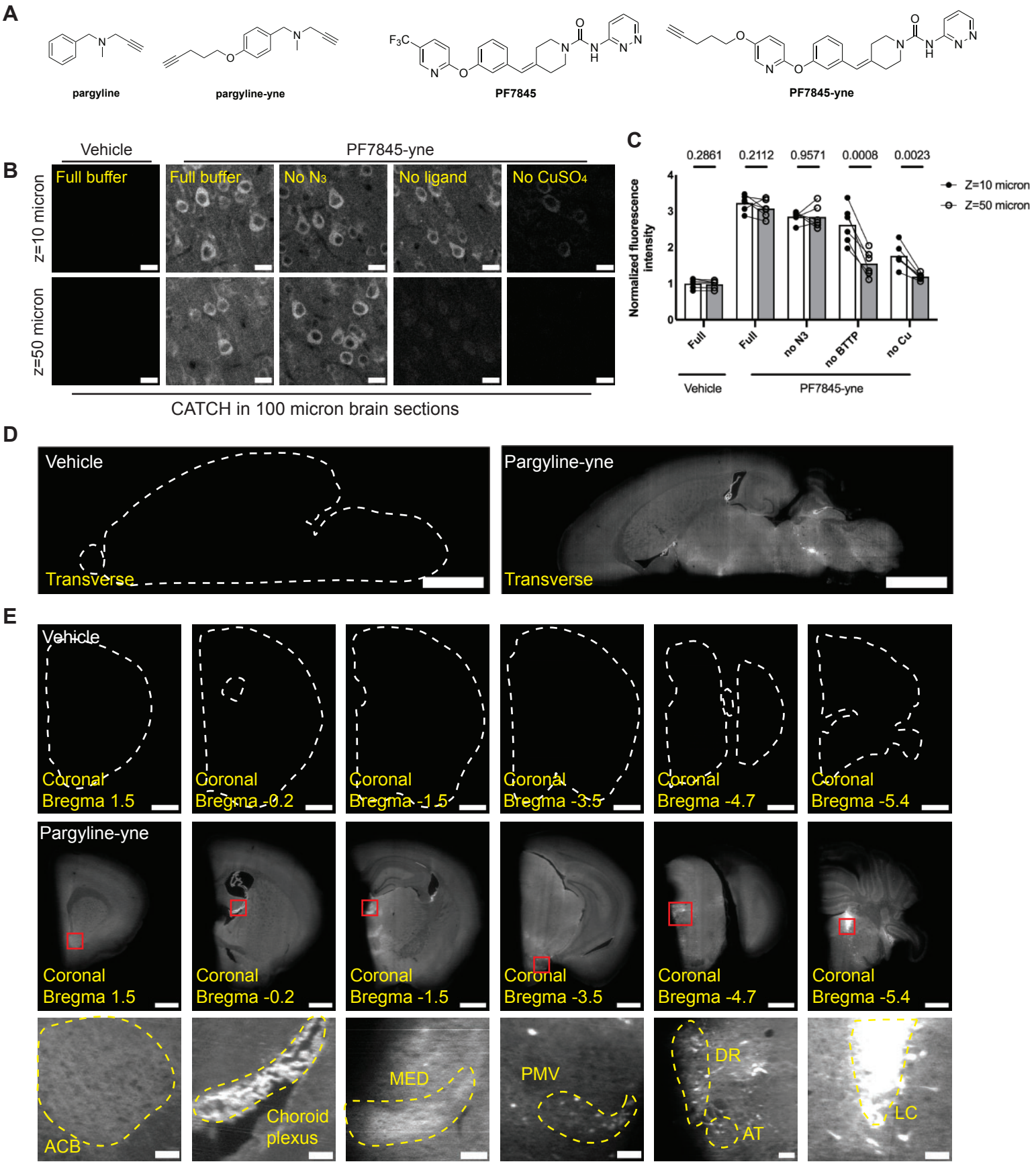
A
pargyline
pargyline-yne
PF7845
PF7845-yne
B
Vehicle
PF7845-yne
Full buffer
Full buffer
No N3
No ligand
No CuSO4
z=10 micron
z=50 micron
CATCH in 100 micron brain sections
C
0.2861
0.2112
0.9571
0.0008
0.0023
Normalized fluorescence intensity
Z=10 micron
Z=50 micron
Full
Full
no N3
no BTTP
no Cu
Vehicle
PF7845-yne
D
Vehicle
Transverse
Pargyline-yne
Transverse
E
Vehicle
Coronal Bregma 1.5
Coronal Bregma -0.2
Coronal Bregma -1.5
Coronal Bregma -3.5
Coronal Bregma -4.7
Coronal Bregma -5.4
Pargyline-yne
Coronal Bregma 1.5
Coronal Bregma -0.2
Coronal Bregma -1.5
Coronal Bregma -3.5
Coronal Bregma -4.7
Coronal Bregma -5.4
ACB
Choroid plexus
MED
PMV
DR
AT
LC

Figure S2

A

Registration | Voxelization and Warping

Pargyline-yne | Vehicle | Pargyline-yne

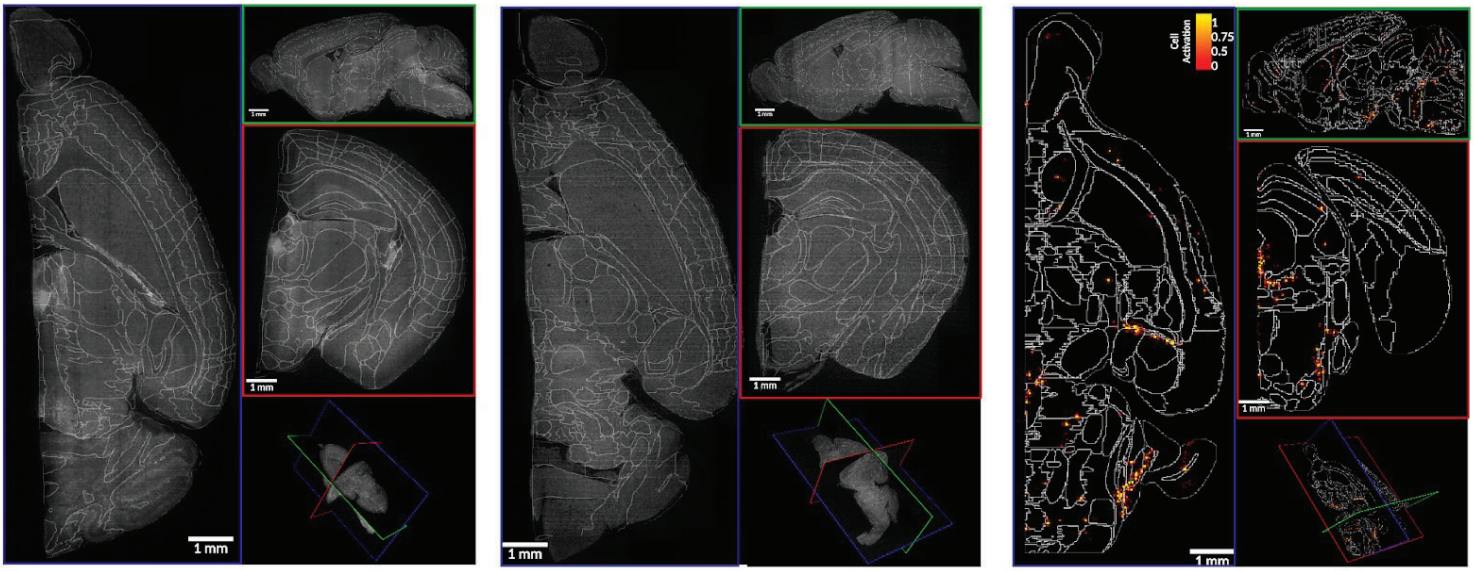

B

Average ***regional intensity*** difference in atlas space

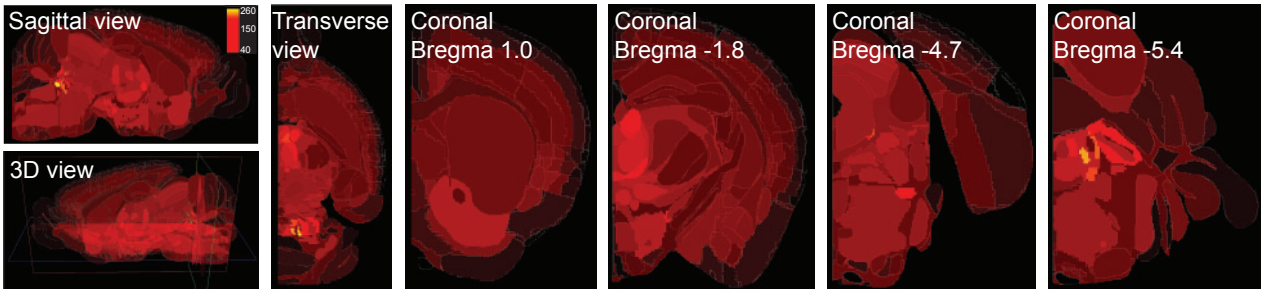

C

Average ***regional neuronal density*** differences in atlas space

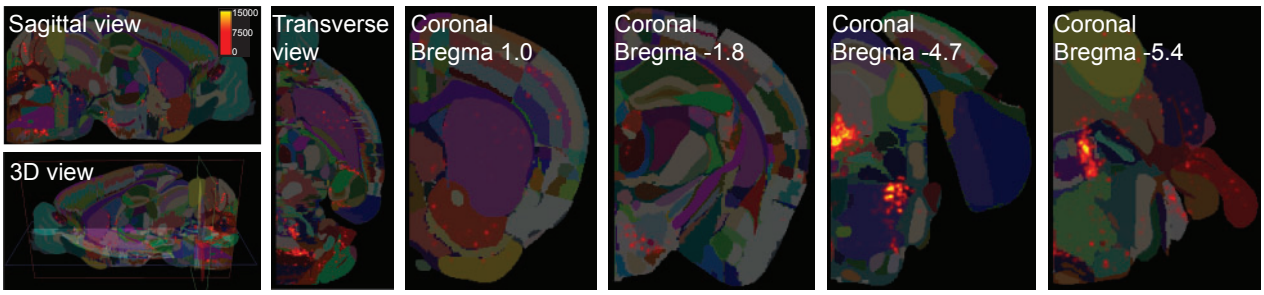

D

Average ***regional neuronal density -log(p-value)*** in atlas space

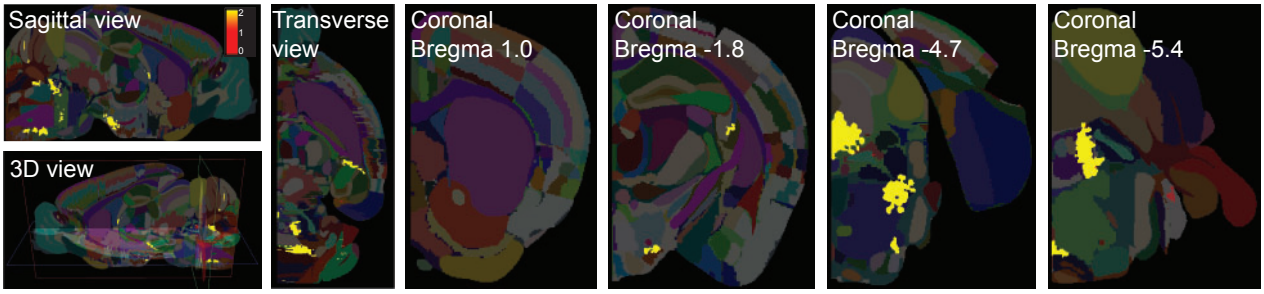

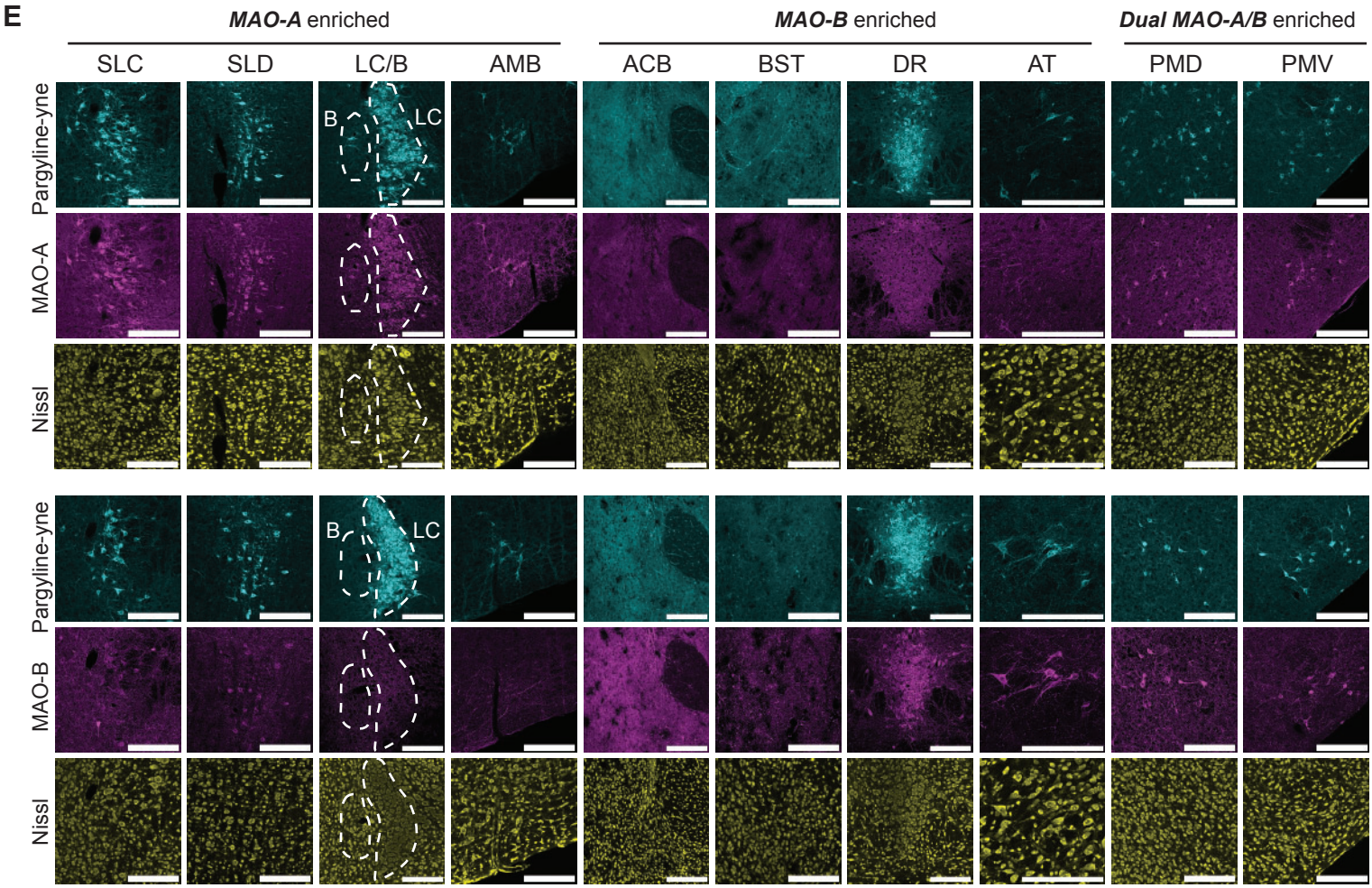
E
MAO-A enriched
MAO-B enriched
Dual MAO-A/B enriched
SLC
SLD
LC/B
AMB
ACB
BST
DR
AT
PMD
PMV
Pargyline-yne
MAO-A
Nissl
B
LC
Pargyline-yne
MAO-B
Nissl
B
LC

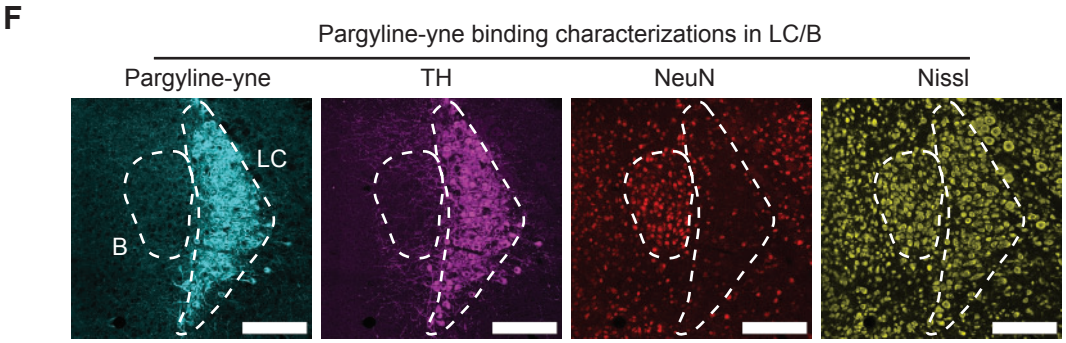
F
Pargyline-yne binding characterizations in LC/B
Pargyline-yne
TH
NeuN
Nissl
LC
B

Figure S3

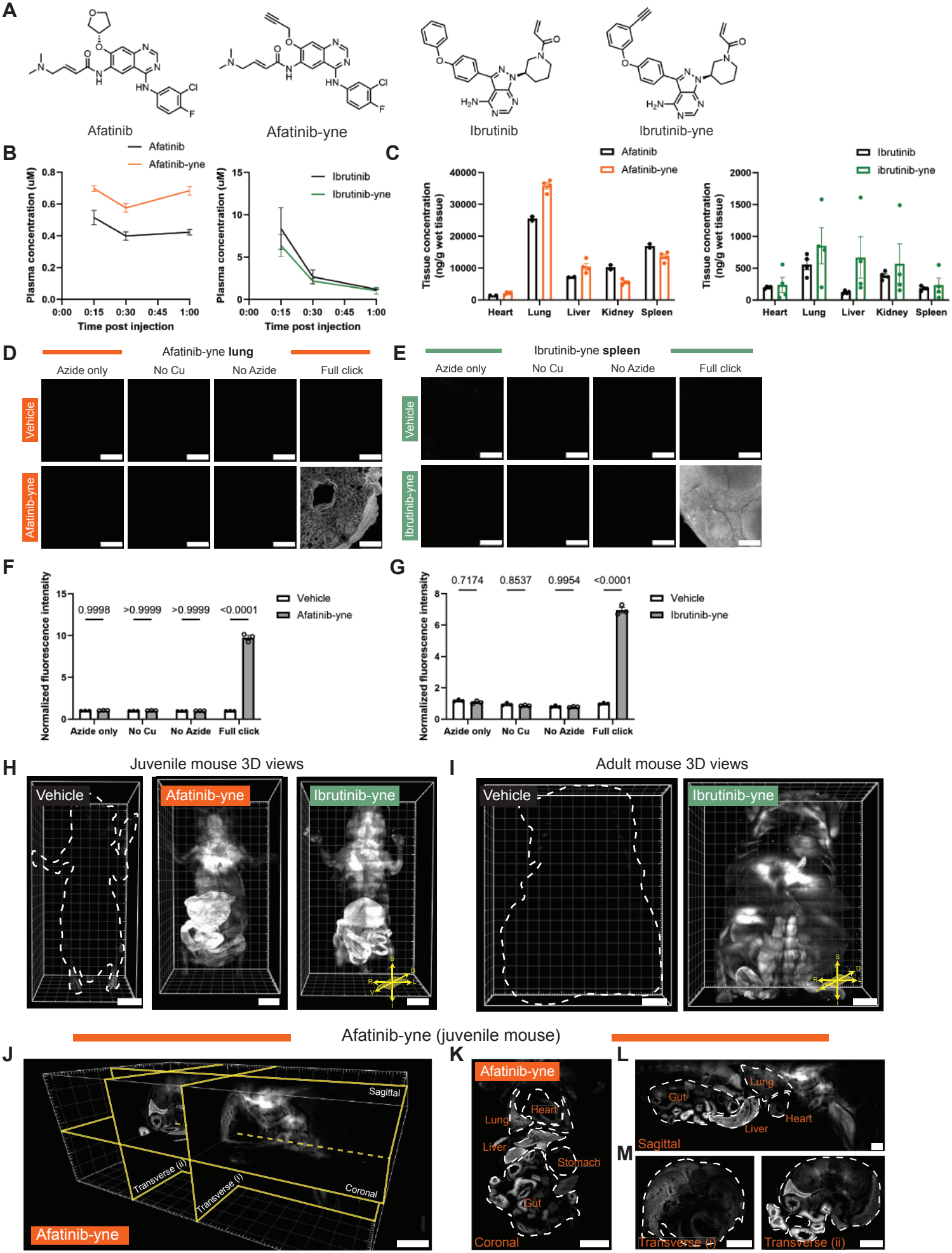
A
Afatinib
Afatinib-yne
Ibrutinib
Ibrutinib-yne
B
Afatinib
Afatinib-yne
Plasma concentration (uM)
Time post injection
Ibrutinib
Ibrutinib-yne
C
Tissue concentration (ng/g wet tissue)
Heart
Lung
Liver
Kidney
Spleen
D
Afatinib-yne lung
Azide only
No Cu
No Azide
Full click
Vehicle
Afatinib-yne
E
Ibrutinib-yne spleen
Ibrutinib-yne
F
Normalized fluorescence intensity
0.9998
>0.9999
>0.9999
<0.0001
G
0.7174
0.8537
0.9954
<0.0001
H
Juvenile mouse 3D views
I
Adult mouse 3D views
J
Afatinib-yne (juvenile mouse)
Sagittal
Transverse (ii)
Transverse (i)
Coronal
K
Lung
Heart
Liver
Stomach
Gut
L
M

Figure S4

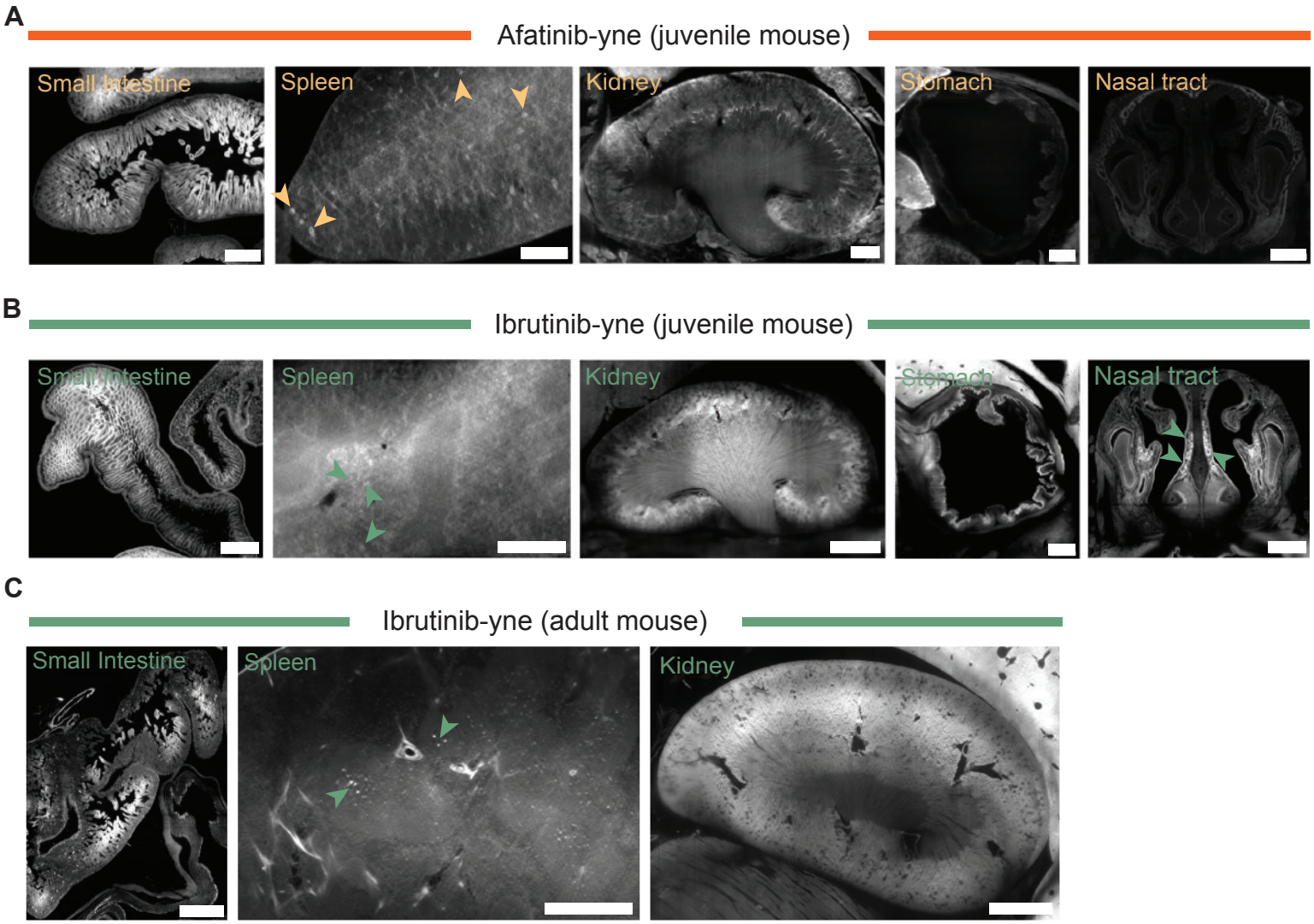
A
Afatinib-yne (juvenile mouse)
Small Intestine
Spleen
Kidney
Stomach
Nasal tract
B
Ibrutinib-yne (juvenile mouse)
Small Intestine
Spleen
Kidney
Stomach
Nasal tract
C
Ibrutinib-yne (adult mouse)
Small Intestine
Spleen
Kidney

Figure S5

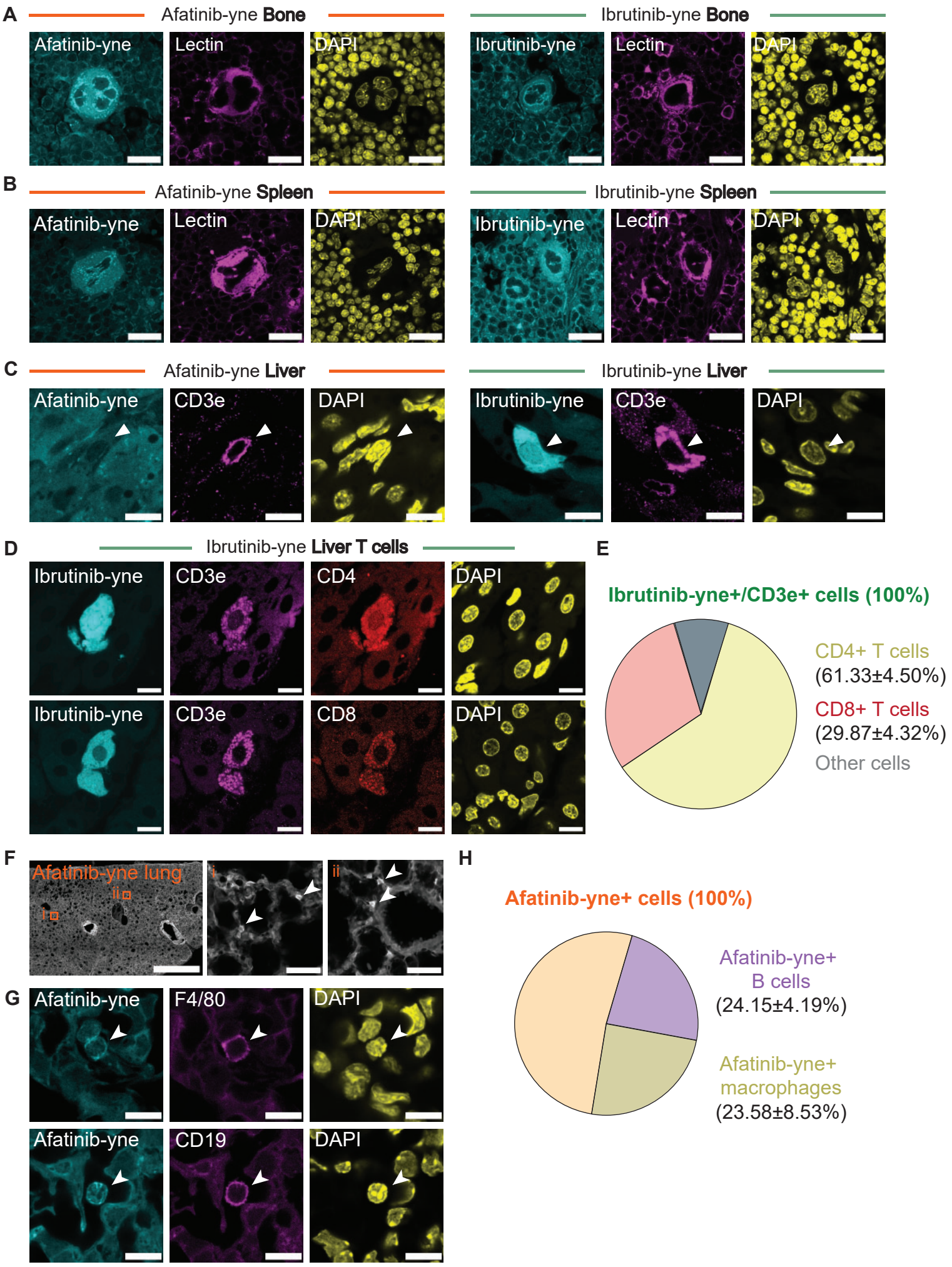
A
Afatinib-yne Bone
Afatinib-yne
Lectin
DAPI
Ibrutinib-yne Bone
Ibrutinib-yne
Lectin
DAPI
B
Afatinib-yne Spleen
Afatinib-yne
Lectin
DAPI
Ibrutinib-yne Spleen
Ibrutinib-yne
Lectin
DAPI
C
Afatinib-yne Liver
Afatinib-yne
CD3e
DAPI
Ibrutinib-yne Liver
Ibrutinib-yne
CD3e
DAPI
D
Ibrutinib-yne Liver T cells
Ibrutinib-yne
CD3e
CD4
DAPI
Ibrutinib-yne
CD3e
CD8
DAPI
E
Ibrutinib-yne+/CD3e+ cells (100%)
CD4+ T cells
(61.33±4.50%)
CD8+ T cells
(29.87±4.32%)
Other cells
F
Afatinib-yne lung
i
ii
G
Afatinib-yne
F4/80
DAPI
Afatinib-yne
CD19
DAPI
H
Afatinib-yne+ cells (100%)
Afatinib-yne+
B cells
(24.15±4.19%)
Afatinib-yne+
macrophages
(23.58±8.53%)